Ref. No. : BV/PKMS/ 219 /2022 -2023

Date : 27/ 06 /2022

To,

The Principal,

Anekant Education Society's,

Jaysingpur College, Jaysingpur.

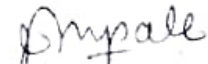**Subject:** Regarding student exchange program under MoU

Respected Sir Madam,

Pursuant to the MoU signed between Anekant Education Society's Jaysingpur College Jaysingpur and Bharati Vidyapeeth's Patangrao Kadam Mahavidyalaya, Sangli. The Ph. D. student Burud Mahesh Dileep (NET-JRF) working under the guidance of Dr. A. R. Supale. Assistant professor P.G. Department of Chemistry Bharati Vidyapeeth's Patangrao Kadam Mahavidyalaya, Sangli. Interested in joining the student exchange program at DST-FIST Laboratory, Jaysingpur College Jaysingpur for research work under the guidance of Co-ordinator DST-FIST laboratory Dr. S. R. Sabale, Assistant Professor. Department of Chemistry Jaysingpur College Jaysingpur.
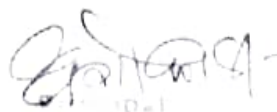
So. kindly request to you do needful.

Thanking you,
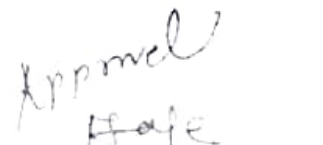
Yours faithfully,

(Dr. A. R. Supale)

Asst. Professor in Chemistry

Forwarded Through:

Vidyapeeth's
Patangrao Kadam Mahavidyalaya Sangli

Approved

Date
27·6·2022

PRINCIPAL
Jaysingpur College Jaysingpur

To,
The Principal,
for permission

Hierarchical Porous Activated Carbon from Wheat Bran Agro-Waste: Applications in Carbon Dioxide Capture, Dye Removal, Oxygen and Hydrogen Evolution Reactions

Amruta Koli,[a] Abhishek Kumar,[b] Akshata Pattanshetti,[a] Amit Supale,[c] Kalyanrao Garadkar,[d] Jian Shen,[e] Jasmin Shaikh,[f] Supareak Praserthdam,[f] Radha Kishan Motkuri,*[b] and Sandip Sabale*[a]

This work reports an efficient method for facile synthesis of hierarchically porous carbon (WB-AC) utilizing wheat bran waste. Obtained carbon showed 2.47 mmol g^{-1} CO$_2$ capture capacity with good CO$_2$/N$_2$ selectivity and 27.35 to 29.90 kJ mol^{-1} isosteric heat of adsorption. Rapid removal of MO dye was observed with a capacity of ~555 mg g^{-1}. Moreover, WB-AC demonstrated a good OER activity with 0.35 V low overpotential at 5 mA cm^{-2} and a Tafel slope of 115 mV dec^{-1}. It also exhibited high electrocatalytic HER activity with 57 mV overpotential at 10 mA cm^{-2} and a Tafel slope of 82.6 mV dec^{-1}. The large SSA (757 m^2 g^{-1}) and total pore volume (0.3696 cm^3 g^{-1}) result from N$_2$ activation contributing to selective CO$_2$ uptake, high and rapid dye removal capacity and superior electrochemical activity (OER/HER), suggesting the use of WB-AC as cost effective adsorbent and metal free electro-catalyst.

Introduction

The global temperature report shows a gradual increase every year since 1951, causing global warming ascribed to the release of various industrial gases, especially carbon dioxide (CO$_2$).[1] The CO$_2$ emissions from industrial, urbanization, and agricultural processes have been recognized as a crucial climate issue. Hence, reducing CO$_2$ emissions before releasing into the environment or capturing them using a proper adsorption technology approach is the need of the present days.[2–4] The Intergovernmental Panel on Climate Change (IPCC) has the ambitious objective of a 50% reduction in CO$_2$ emissions by 2050, and to meet the required goal cost-effectively, carbon capture and storage technologies need to contribute at least one-fifth of the target.[5]

Likewise, the growing industrialization and urbanization predominantly cause water pollution due to the discharge of various hazardous pollutants, including pesticides, fertilizers, microplastics, detergents, drugs, dyes, etc.[6–8] Among these pollutants, dyes used in textile industries have been categorized as a major source of water pollution.[9] Among the synthetic dyes used in textile industries, azo dyes are mostly preferred due to their extremely high molar extinction arising from azo linkage (—N≡N—).[10] The aromatic and azo groups present in such dye are highly toxic and, carcinogenic and harmful to both humans as well as to the ecology.[11,12] Methyl orange (MO) is one such dye commonly used in the textile industry that requires the immediate attention of researchers.[13] These factors have garnered researchers' attention to removing dyes before releasing them into water bodies or treating the polluted water by eliminating the dyes.[14,15] Adsorption technology is preferred over other methods for dye removal, such as membrane separation, flocculation sedimentation, oxidative degradation, etc., due to the simplicity, cost-effectiveness, efficiency, and selectivity offered by various adsorbents.[16,17]

Equally, the growing energy needs, exhaustion of non-renewable resources, and global warming associated with environmental issues have attracted attention in the realms of renewable energy.[18] The electrochemical processes, hydrogen evolution reaction (HER) and oxygen evolution reaction (OER) have gained substantial interest, which includes two half-cell reactions of O$_2$ and H$_2$ evolution.[19] The OER or HER process has

[a] Dr. A. Koli, A. Pattanshetti, Dr. S. Sabale
Department of Chemistry
Jaysingpur College
Jaysingpur 416101 (India)
E-mail: srsabale@gmail.com

[b] Dr. A. Kumar, Dr. R. K. Motkuri
Energy and Environment Directorate
Pacific Northwest National Laboratory
Richland, WA, USA
E-mail: RadhaKishan.Motkuri@pnnl.gov

[c] Dr. A. Supale
Dr. Patangrao Kadam Mahavidhyalaya College
Sangli-416416 (India)

[d] Prof. Dr. K. Garadkar
Department of Chemistry
Shivaji University
Kolhapur 416004 (India)

[e] Dr. J. Shen
College of Environment and Resources
Xiangtan University
Xiangtan 411105 (China)

[f] Dr. J. Shaikh, Prof. Dr. S. Praserthdam
Department of Chemical Engineering Faculty of Engineering
Chulalongkorn University
Bangkok 10330 (Thailand)

a major challenge because this process follows multistep proton-coupled electron transfer, leading to slow reaction kinetics. Catalysts required for this reaction are expensive. Various catalysts, such as noble metals (Ru, Ir, Pt and their oxides), are fabricated to date that act as very competent OER and HER catalysts due to low overpotentials and fast reaction kinetics.[20] However, their large expense obstructs a wide range of applications. Henceforth, the discovery of abundant, productive, and economical catalysts is crucial for practical applications.[21]

For global CO_2 and dye emission issues, the adsorption technology using solid porous adsorbents has played a key role in recent years that employs zeolites, metal-organic frameworks (MOFs), porous polymers, and silica-based materials, as well as porous AC (PACs).[22–26] Among these porous solid adsorbents, PACs are considered potential materials for CO_2 capture and dye removal applications due to their large and manipulating SSA, pore structure and volume, mechanical properties, and excellent operability at different experimental conditions.[27] The large SSA with a lot of micropores produced by PAC also encourages the charge transfer of OER or HER at their surface. Hence, the development of efficient metal-free electrocatalysts with low overpotential at reasonable cost and significant stability is very crucial for practical applicability.[28] However, easy production and raw material availability make them cost-effective over other porous materials.[29,30] The agro-waste is one of the alternatives to produce PACs employing physical or chemical approaches, including acid carbonization, N_2 activation, KOH/Na_2CO_3 activation, etc.[31] Apart from being effective in pollutant removal, the PACs derived from agro-waste are economical due to the abundantly available agro-waste.[32]

Wheat bran (WB) is one of the major agricultural by-products with great potential for turning into a high-value-added product such as PACs. About a quarter ton of WB is produced from one ton of wheat,[33] and around ~190 million tons of WB were produced last year, considering around 776 million tons of wheat were produced in 2020–21. In this work, we have aimed to utilize WB agro-waste as a source for producing PACs (WB-AC) employing H_2SO_4 carbonizing followed by N_2 activation. This work aims to resolve the CO_2 capture, dye removal, and energy (OER/HER) applications using low-cost WB-AC. The MO dye is selected as the model for the dye removal

studies. To the best of our knowledge, this is the first study for WB-derived PACs for dual application of CO_2 capture and dye remediation. This study presents a detailed study on CO_2 capture, selectivity, adsorption isotherms, MO removal capacity, equilibrium, and adsorption mechanism based on the adsorption kinetic and isothermal models. Furthermore, WB-AC demonstrated remarkable electrochemical activity towards both OER and HER catalysis having low-onset potential and over-potential (η), small Tafel value, and long-term stability.

Results and Discussion

The present study aims to prepare a low-cost porous carbon material from inexpensive and readily available agro-waste, WB. A well reported chemical carbonization methods were used to obtain the final porous carbon material. First, the chemical carbonization of WB was performed using concentrated H_2SO_4, where treatment of WB with H_2SO_4 leads to dehydration of cellulose, resulting in the formation of porous WB-RC.[34,35] Thus, the obtained WB-RC was subjected to activated under N_2 at 773 K for 2 h to get porous WB-AC material. The decomposition of volatile matter results in the formation of hierarchical pores in WB-AC mainly due to N_2 activation treatment. The yield of WB-RC and WB-AC was found to be 50% and 45%, respectively. This yield is quite low because the wheat bran is soft agro-waste owing to its better properties of pore structures due to the composition. Scheme 1 summarizes the steps involved in the synthesis of WB-AC. Both physical and chemical activation methods are reported for synthesizing high porous materials.[31,36] However, it was observed that the physical activation method is most adaptable and considered eco-friendly due to the absence of chemicals during the activation process.

The structure and degree of crystallinity of the obtained WB-RC and WB-AC materials were studied by powder X-ray diffraction (PXRD) patterns (Figure 1a). It is clearly observed that both the materials displayed a diffused curve lacking significant peak intensity around 23° and 42°, corresponding to the (002) and (100) crystal planes, respectively. The existence of broad peaks indicates that the crystalline structures of WB (Figure S1) have disappeared after carbonization and activation, which are
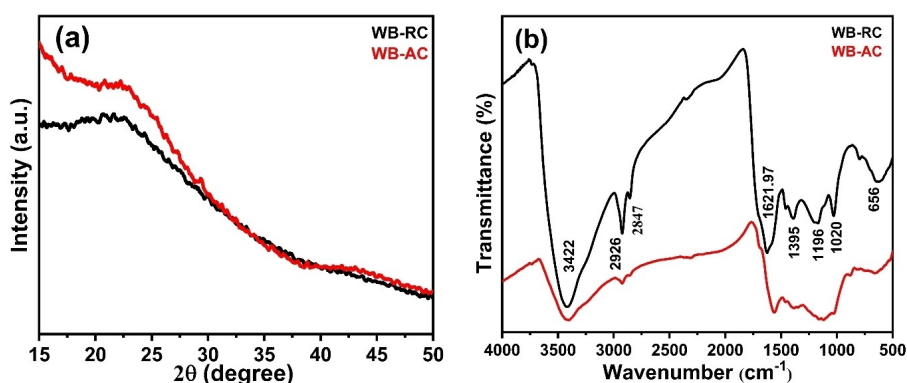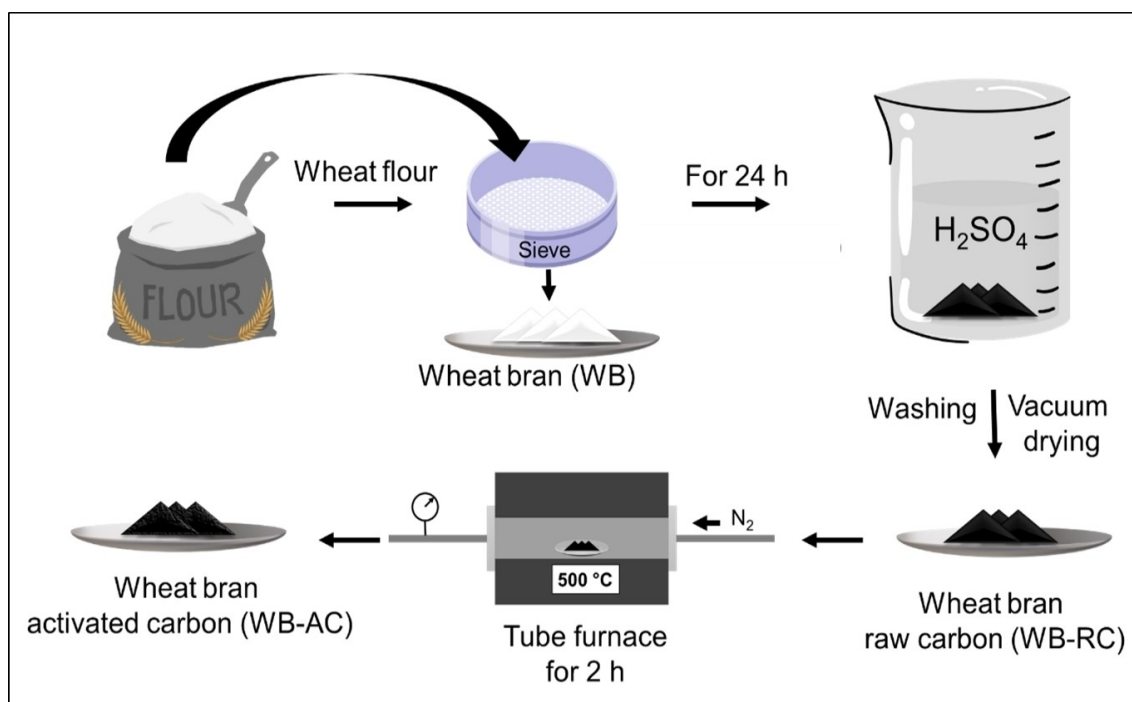

Figure 1. (a) XRD pattern and (b) FT-IR spectra of WB-RC and WB-AC.

ChemPlusChem

Research Article
doi.org/10.1002/cplu.202300373

Chemistry Europe
European Chemical
Societies Publishing

Scheme 1. Synthesis route of hierarchical porous AC from WB

reflected in the amorphous domain.[37] The WB-AC with large d-spacing comparable with WB-RC proves that small primary mesopore sizes and considerable amounts of micropores. Moreover, the peak at 42° in WB-RC completely disappeared, and the relative intensity for the peak at 21° is slightly weaker than the WB-AC. This suggests that relative intensity for the broad peak 42° in WB-AC reveals that N_2 activation moderately shrinks the inner layer spacing or increases the degree of graphitization in WB-AC and carbon-rich amorphous structure.

Besides the carbon atoms, heteroatoms like H, O and N are present in the prepared carbons (Table S1), which may be helpful in establishing their applications. The elemental composition of these heteroatoms was determined from CHN and confirmed using XPS analysis. In the present study, the C content in WB-RC is 29.31% on average, representing an increase of C content of about 75.46% with respect to WB-AC. This makes the WB-AC an excellent material because the C content is one of the important organic matter for the development of material with a high SSA and porosity.[38] The WB-AC showed a reduction in H contents compared to WB-RC, associated with the release of volatile matter during activation, which was validated by FTIR analysis.

The FTIR spectra (Figure 1b) of WB-RC and WB-AC reveal that both materials have the same kind of surface groups. The characteristic peak observed at 3422.25 cm^{-1} for WB-RC was mainly due to surface hydroxyl or amine functionality (O–H or N–H stretching). The characteristic peaks observed at 2926 cm^{-1} and 2847 cm^{-1} are mainly due to asymmetric and symmetric vibrations (C–H stretching). The thermal treatment could remove the contents of aliphatic groups in WB-AC,[39] which is attributed to the decrease in intensity of the peak in WB-AC.

The peak observed at 1621.97 cm^{-1} is assigned to the stretching vibration of carbonyl (C=O stretching). The peaks centered at 1395 cm^{-1} and 1196 cm^{-1} are mainly due to the scissoring or bending vibration of –C–H bonds or =C–H bending vibration in alkane groups. The peak at 1020 cm^{-1} is related to the C–N stretch (aliphatic amines).[40,41] The peak at 656 cm^{-1} is attributed to the cut-off plane bending vibrations of –CH bonds. The same peaks with low intensity are observed in WB-AC, which confirms WB-RC conversion into AC. However, the FT-IR observations showed the mere presence of active sites could be significant for CO_2 uptake and MO adsorption capacity.

To obtain brief information about the change in morphology of the WB-RC material, FE-SEM analysis of both samples was performed (Figure 2). The surface of WB-RC exhibited scattered cavities (Figure 2a), whereas WB-AC (Figure 2b) exhibits holes on the rough surface along with cracks and crevices, which show heterogeneous surface morphology by opening pore cavities with well-organized honeycomb-like pore structure, resulting in abundant micro and mesopores in the material (supported by BET results). This result confirms that activation leads to the formation of a porous structure. In addition, an abundance of micropores also provides favorable and more efficient paths for high-performance adsorbent.[42]

Figure 2c shows the N_2 adsorption-desorption isotherms and the pore size distribution (Figure 2d) of the synthesized carbon materials at 77 K. As illustrated in Figure 2d, WB-RC exhibits a type I adsorption isotherm at a swift curve at low relative pressure, suggesting the homogenous microporous structure. However, WB-AC is classified as type IV, along with a slight H4 hysteresis loop, which indicates the characteristic mesoporous nature, according to IUPAC.[43,44] Furthermore, the
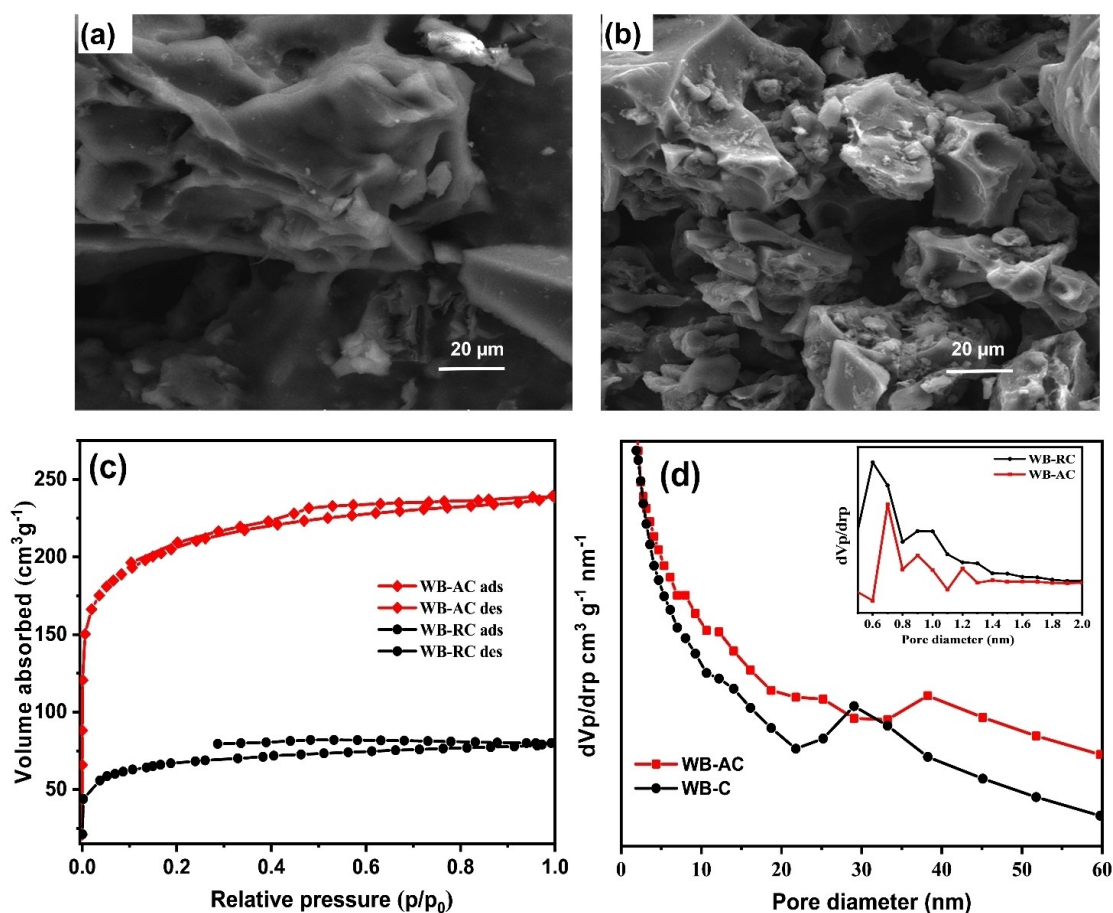
ChemPlusChem

Research Article
doi.org/10.1002/cplu.202300373

Chemistry Europe
European Chemical
Societies Publishing

Figure 2. Morphological characterizations of the WB-RC and WB-AC; FE-SEM images of WB-RC (a) and WB-AC (b) with magnification 20 μm, respectively, N_2 adsorption/desorption isotherm at 77 K for the WB-RC and WB-AC, (c) and Total pore size distribution curve calculated using Barret-Joyner-Holanda (BJH) method (d) (inset: micropore region).

appearance of hysteresis loops in the relative pressure of 0.5 indicates the presence of certain mesopores with a capillary condensation ($p/p_o > 0.4$). In the relative pressure range of 0–0.45 p/p_o the WB-AC isotherm shows a soft curve due to the appearance of larger pores, leading to a delay in monolayer formation. Also, the high curvature of isotherm lap at lower relative pressure and an increase in N_2 adsorption by enhancing the pressure are attributed to the expansion of micropore structure, which is supported by the PSD curves as well as the morphology of material demonstrated from FE-SEM. As shown in Figure 2d, the PSD of the material indicates the existence of both micro (diameter < 2 nm) and mesopores ($2 <$ diameter < 50 nm), showing hierarchical porosity. The micropore size is confirmed by the MP plot, as shown in Figure 2d (inset image). Both carbons have a well-defined pore system in the micropore range; however, the microporosity of WB-AC increases with a maximum pore size of 0.7 nm than 0.59 nm in WB-RC, which demonstrates pore broadening due to N_2 activation, which may be useful in the enhancement of CO_2 uptake and dye adsorption properties. Xiong et al. demonstrated that pores smaller than 0.8 nm are highly effective for CO_2 uptake due to strong CO_2–adsorbent interactions.[45] Considering this fact, WB-

AC showed enhanced CO_2 capture capacity and MO adsorption performance compared to the WB-RC sample.

Prior to the measurement of an adsorption isotherm, all the physisorbed species should be removed from the surface of the material. This may be achieved by degassing the surface to a high vacuum at elevated temperatures. The total N_2 uptake in WB-RC and WB-AC reached 56.54 and 174.08 $cm^3 g^{-1}$, respectively, where comparatively high nitrogen uptake at the low pressure range in WB-AC is attributed to the micropore-filling mechanism.[46] The BET and Langmuir SSA calculated from plotted isotherms are 246 and 322 $m^2 g^{-1}$ for WB-RC and 757 and 1041 $m^2 g^{-1}$ for WB-AC. The total pore volume (micropore volume) of WB-RC and AC was found to be 0.1237 (0.03556) and 0.3696 (0.09603) $cm^3 g^{-1}$, respectively. Therefore, it is suggested that the N_2 activation significantly introduces porosity in WB-AC, which leads to the maximum SSA and pore volume (as summarized in Table S2) to access the whole surface for efficient adsorption capacity. Therefore, besides SSA, some aspects play vital roles in adsorption performance; primarily, pore size is considered a crucial effect. According to the microporous analysis, both WB-RC and WB-AC have a smaller micropore which was calculated using MP plot. But compared

ChemPlusChem

Research Article
doi.org/10.1002/cplu.202300373

**Chemistry
Europe**
European Chemical
Societies Publishing

with WB-RC, WB-AC contains high microporosity, which may be more favorable to the adsorption.

The XPS analysis was achieved to confirm the surface functionality as well as to confirm the elemental composition of the obtained materials. The analyzed C 1s and O 1s spectra are deconvoluted and fitted using the Gaussian fitting method. Both WB-RC and WB-AC show three distinguished peaks, representing the C, H and N groups (Figure 3). The XPS survey spectrum of WB-RC and WB-AC (Figures 3a and 3b) showed the C1s peak at 284.8 eV, the O1s peak at 532.1 eV, and the smaller N1s peak between 399–401 eV. The C1s peak can be resolved into four peaks centered at binding energies of 284.5, 285.2, 286.2, and 288.8 eV representing sp^2 C=C (C_1), sp^3 C–C (C_2), C–O/C–N (C_3) and -COOH (C_4) respectively were observed in WB-RC (Figure 3c). In the case of WB-AC, peaks at about 284.8, 285.5, and 287.8 can be assigned to the binding energy of sp^2 C=C (C_5), sp^3 C–C (C_6), and O–C=O (C_7), respectively[47] (Figure 3d). In WB-RC, the kinetic energy of the emitted photoelectron is reduced, with the difference corresponding to the energy change between the ground state and the excited state. This results in establishing a satellite peak: a few electron volts lesser in kinetic energy than the main peak, which gives the characteristic shake-up line for C that may occur in aromatic compounds, a shake-up process involving the energy of the π-

π* transition, as shown in Figure 3d. The high resolution of the O 1s spectrum of WB-RC (Figure S2a.) materials fitted with four peaks, which reveals the appearance of peaks corresponding to quinolinic (O1), C=O (O_2), O–H (O_3), and C–O–C (O_4), located at 530.9, 531.7, 532.6 and 533.7 eV respectively. The WB-AC (Figure S2b) fitted with four peaks rather than quinolinic, attributed to C=O (O_5), O–H (O_6), and C–O–C (O_7) located at the same binding energies, additionally, a small content of water cluster (O_8) peak located at 535.8 eV.[48,49] Compared with WB-RC, the C content in WB-AC increased from 64.1% to 87.7%, and the oxygen content decreased from 32.5% to 11.8%, indicating oxygen-containing functional groups were decomposed during the activation. Furthermore, based on the chemical composition of the WB-AC, the N containing functional groups, acid–base interaction between adsorbate and WB-AC, which is beneficial to adsorption performance. In addition to textural properties, adsorption performance can also be linked to surface interactions, including acid–base interaction, polar interaction, and hydrogen bonding between adsorbate and N containing functionality. These factors also play an important role in the field of energy, therefore prepared WB-AC acts as excellent electrode material. The π-π dispersive interactions promotes accessibility to surface area.[50] Indeed, the activation increases graphitization while widening the
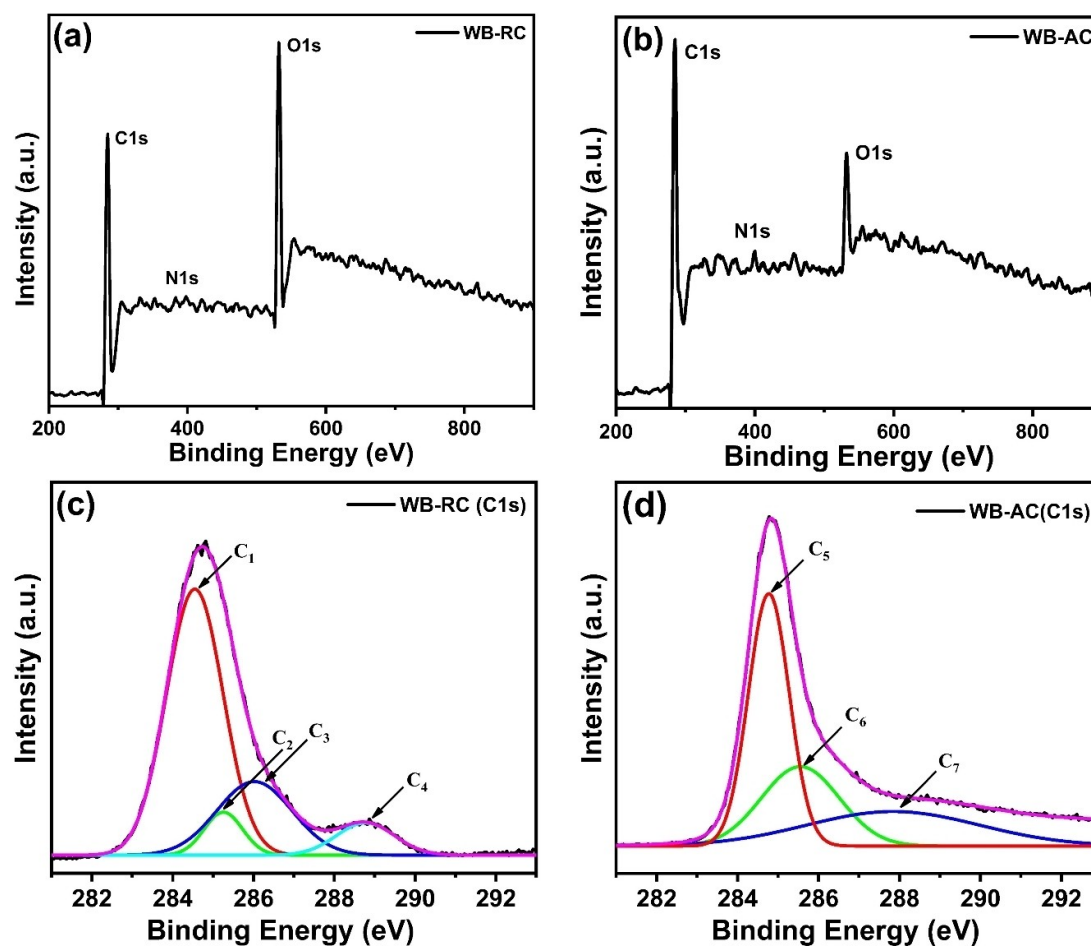

Figure 3. Survey XPS and C1s XPS spectrum of WB-RC (a) and (c); and of WB-AC (b) and (d) respectively
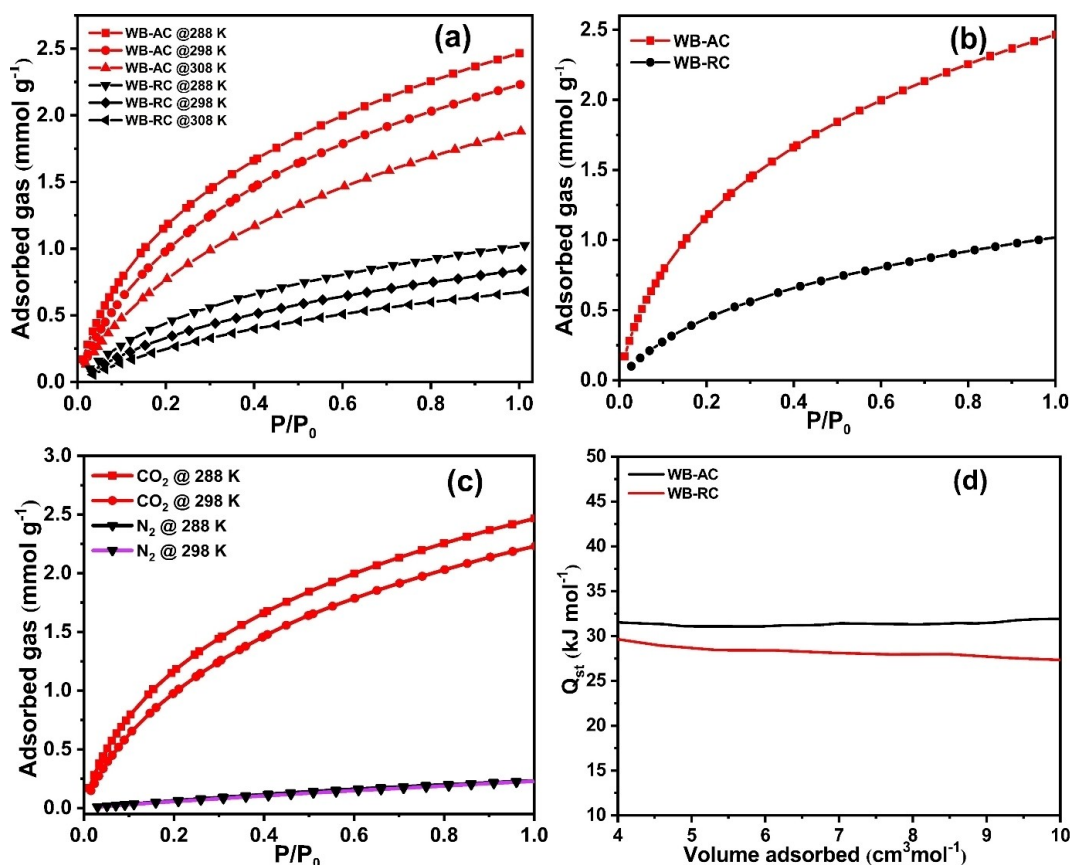
Figure 4. Gas adsorption performances (a) CO_2 adsorption amount of WB-AC and WB-RC at 288 K, 298 K and 308 K, (b) Comparative CO_2 adsorption amount of WB-AC and WB-RC at 288 K, (c) Henry's law CO_2/N_2 selectivity of WB-AC at 288 K and 298 K, (d) Isosteric heat of adsorption (Qst) calculated using the Clausius−Clapeyron equation, based upon the CO_2 adsorption isotherms at 288 K and 298 K.

micropore width. This attributes that the graphitization of C occurs, which was supported by XRD analysis.

The CO_2 adsorption experiments are carried out using the volumetric method under 1 atm pressure at 288, 298, and 308 K. The adsorbent WB-AC, formulated in this work, exhibits high CO_2 capture potential and results in 2.47 mmol g^{-1} CO_2 adsorption compared to WB-RC (1.02 mmol g^{-1}). This enhancement in the CO_2 capture efficiency is owing to superior microporosity, pore volume, and high SSA (757 m^2 g^{-1}) of WB-AC over WB-RC (246 m^2 g^{-1}). Therefore, the enhancement in the SSA and pore volume due to N_2 activation plays an important role in the production of AC adsorbents by increasing adsorption sites for CO_2. The obtained CO_2 adsorption isotherms of WB-RC and WB-AC at 288, 298, and 308 K under 1 atm pressure are given in Figures 4a and 4b; however, CO_2 adsorption capacity is presented in Table 1. As shown in Figure 4, the CO_2 capacity ranges from 0.10 to 1.03 mmol g^{-1} for WB-RC and 0.17 to 2.47 mmol g^{-1} for WB-AC at 288 K. As reported in the literature, the amount of CO_2 adsorption is directly related to the presence of microporosity; here the enhancement in the microporosity of WB-AC results in high CO_2 adsorption capacity (Table 1). The findings indicate that high SSA and more micropores/less mesopores are the prime parameters in designing hierarchical porous carbons for enhanced adsorption capacity.[46,51,52]

Table 1. CO_2 adsorption performance of WB-RC and WB-AC (at 1 atm P)

Sample	BET surface area (m^2 g^{-1})	Adsorption capacity (mmol g^{-1})	T (K)
WB−RC	246	1.03	288
		0.84	298
		0.68	308
WB−AC	757	2.47	288
		2.23	298
		1.88	308

The interaction strength between CO_2 and carbon materials was further evaluated by its isosteric heat of adsorption (Qst) (Figure 4d). The WB-AC shows a high Qst, which ranges from 27.35 to 29.90 kJ mol^{-1}. The Qst decreases rapidly with an increase in CO_2 adsorption; the non-uniformity of Qst over the entire range of CO_2 adsorption suggests the heterogeneous adsorption sites in the adsorbent. The heterogeneity can occur at lower CO_2 adsorption loading in WB-RC. This suggests the non-existence of strong interaction between CO_2-adsorbent, which is evidenced by the decrease in Qst. The greater Qst at low CO_2 loading is conceivable than the interactions between CO_2 and the basic N functionalities enhancement in pores. The fitting results obtained from different models are summarised

ChemPlusChem

Research Article
doi.org/10.1002/cplu.202300373

Chemistry Europe
European Chemical
Societies Publishing

in (Figures S3, S4, S5, and S6), with the highest correlation coefficient ($R^2 = 0.9999$) for the CO_2 adsorption on WB-AC. The Q_{st} was calculated by applying a Clausius–Clapeyron equation (Eq. S1) to these fittings. The absolute component loadings were good fitted with a dual-site Langmuir model.[53–55]

Besides good adsorption capacity, high selectivity against N_2 gas is another important property of a superior CO_2 adsorbent. As shown in Figure 4c, the adsorption capacity for N_2 is much lower than that of CO_2 at 288 and 298 K. The CO_2/N_2 selectivity acquired from Henry's law was employed utilizing the virial equation to fit the CO_2 and N_2 adsorption isotherms to predict the gas mixture adsorption behavior (ESI: detailed calculation, figs. S7, S8, and table S3).[23,56] For this purpose, the adsorption capacity of N_2 was measured at 288 and 298 K, which contains a lower value of adsorption capacity than CO_2, reaching a maximum of 0.23 mmol g^{-1} at 288 K and 1 atm. Therefore, WB-AC could be considered a more selective adsorbent for CO_2 and N_2 separation. The WB-AC exhibits high adsorption selectivity 40.10 for CO_2 over N_2 at 288 K and 32.22 at 298 K. This greater affinity may be ascribed to its plentiful micropores along with mesopores and the presence of many heteroatoms.[45,57] Table S4 summarizes and compares the properties of WB-AC for CO_2 capture with other agro-waste-derived PACs.

The MO dye is used as a model organic pollutant to examine the applicability of the AC for effluent treatment applicability. The contact time and initial MO solution concentration, including the equilibrium and the maximum adsorption capacity, are key factors in the adsorption process as they affect the adsorption capability of adsorbents.[58,59] As shown in Figure 5a, the adsorption equilibrium of 10 mg L^{-1} MO was almost achieved after 20 min. It is clearly noted that a higher concentration of dye solution at an equilibrium could achieve a larger amount of MO adsorption. The maximum adsorption capacity of WB-AC was found to be 555 mg g^{-1} at 200 mg L^{-1} MO concentration. The increase in the adsorption capacity may be due to the increase in the number of adsorption sites due to area. However, it is observed that the dye removal capacity is slowly decreased after adsorption equilibrium (200 mg L^{-1}). This decrease in adsorption removal capacity may be due to the adsorbent particles' agglomeration, which reduces the effective number of adsorption sites.

The equilibrium adsorption capacity (q_e) of the WB-AC was calculated using Eq. S8. The equilibrium adsorption data were plotted and fitted using adsorption isotherm models such as Langmuir (Eq. 1), Freundlich (Eq. 2), and Temkin (Eq. 3) isotherms, which provide information about the adsorption system
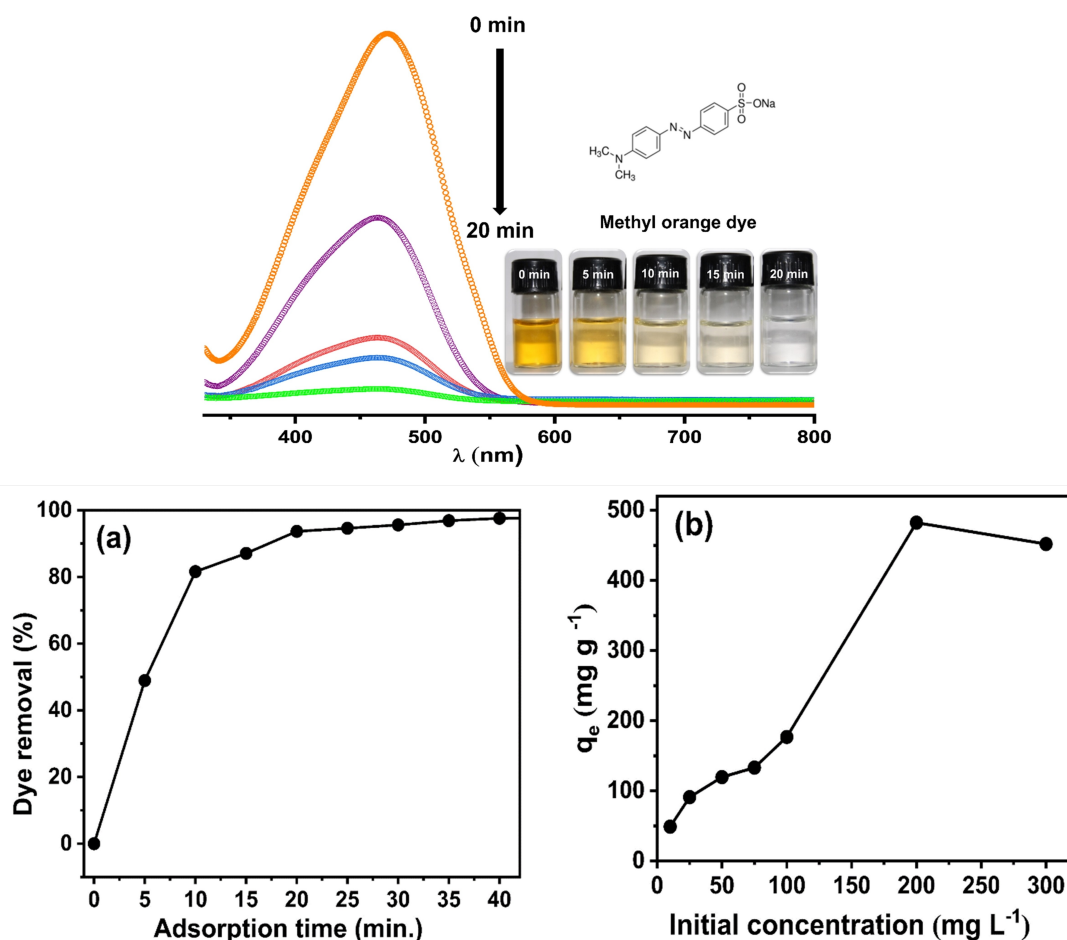

Figure 5. UV-Vis spectra of MO dye adsorption on WB-AC w.r.t time (10 mg L^{-1}, 0 to 20 min), (a) % dye removal and (b) Equilibrium adsorption capacity of WB-AC for MO.

ChemPlusChem

Research Article
doi.org/10.1002/cplu.202300373

Chemistry Europe
European Chemical
Societies Publishing

and relationship between adsorbent (WB-AC) and MO concentration.[60–62]

$$\frac{C_e}{q_e} = \frac{1}{bq_m} + \frac{C_e}{q_m} \tag{1}$$

$$\ln q_e = \ln k + \frac{1}{n}\ln C_e \tag{2}$$

$$q_e = B\ln(A_T\, C_e) \tag{3}$$

where q_e and C_e are the same parameters described in Eq. S8, the K_F and K_T are constants. Freundlich constant K_F is related to the MO loading on the adsorbent, and $1/n$ is another constant that is sensitive to the heterogeneity of the WB-AC surface. This system is more heterogeneous because the n value is 2.64, which usually results in the non-linearity of the adsorption isotherm. The adsorption isotherm values calculated from different isotherm models are provided in Table 2, which predicts adsorption equilibria. Among three isotherm models, the Freundlich isotherm model showed a good correlation coefficient ($R^2 = 0.8223$), which suggests the formation of a monomolecular layer of MO on the WB-AC surface (Figure S10b), the maximum MO adsorption capacity of the WB-AC was found to be 555 mg g^{-1}.

The understanding of the adsorption kinetics of MO on the WB-AC was calculated using Eq. S9 and Eq. S10 with the help of two kinetic models, pseudo-first order and pseudo-second order. The concentration plot of adsorbed MO versus contact time is shown in Figure 5b, where the R^2 coefficients of determination were obtained to be 0.9198 and 0.9727 for pseudo-first-order and pseudo-second-order models, respectively (Figure S9). The equilibrium adsorption time (qt) was calculated by the pseudo-second-order model (95.19 mg g^{-1}), which suggests a good agreement with experimental data (91.0 mg g^{-1}) (Table S5). The data recommend the suitability of a pseudo-second-order kinetic model to describe the MO adsorption phenomenon.

The WB-AC showed a high MO adsorption capacity; therefore, recycling performance was carried out. After the first cycle, the WB-AC was separated, and a minute quantity was lost after every cycle, because the WB-AC is very porous and lighter therefore, recovery of the material was quite difficult. It was successfully recovered through a 0.22-μm nylon syringe. The recyclability of WB-AC was carried out by using reactivation at 773 K for 60 min. In the first cycle of regeneration study about 97.68% of MO was removed and about 88.02% MO was removed in 2nd cycle. Later, in the 3rd cycle, the % removal of MO is decreased to about 71.25%, as shown in Figure 6. This
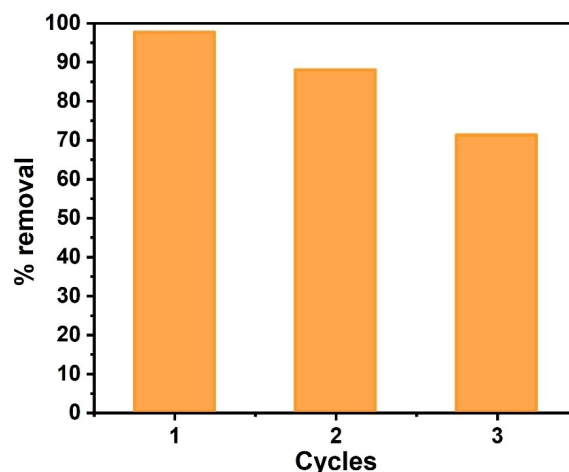

Figure 6. Recycling performance of WB-AC

loss may be due to the blockage of active sites as well as the loss of material. However, considering the loss of material and its subsequent removal efficiency %, the recyclability of WB-AC is noticeable. Table S6 compares the dye adsorption capacity of WB-AC with other agro-waste-derived PACs.

To evaluate the electrocatalytic performance of WB-AC, the electrochemical work was performed in 1.0 M KOH using three-electrode set-up. The electrochemical performance of the WB-AC was primarily characterized by cyclic voltammetry (CV). The CVs of WB-AC are measured in the potential of −0.3 to 0.3 V with a scan rate of 100 mV s^{-1} using 1.0 M KOH aqueous electrolyte saturated with N$_2$. Working electrodes are scanned for 1000 potential cycles for both OER and HER activities until the signals are stabilized (Figure S11a). After 1000 cycle's CV curve exhibits a typical quasi rectangular shape and no obvious electrochemical features analogous to faradic current are observed.

The polarization curves were recorded by linear sweep voltammogram (LSV) measurements at a scan rate of 10 mV s^{-1} in 1.0 M KOH to analyze the electrocatalytic OER performance. Figure 7a shows LSV curves with iR compensation performed in 1.0 to 1.8 V vs. RHE. The weak anodic waves at ~1.54 V belong to Ni foam, corresponding to the redox potential of Ni(II)/Ni(III).[63] The WB-AC electrode delivered low overpotentials of 0.35 V and 0.48 V with the OER onset potential achieved at ~1.58 V, and 1.71 V at 5.0 and 10 mA cm^{-2}, respectively. This onset potential is slightly lower than the IrO$_2$ (1.79 V) catalysts, demonstrating the significance of agro-waste derived AC.[64]

The tafel plot is an important study to investigate the kinetics of OER electrocatalytic material; this gives insight and

Table 2. Isotherm values for adsorption of MO onto WB-AC at Equilibrium. Adsorption isotherm values like maximum adsorption capacity (q_{max}), Langmuir constant (K_L), Freundlich parameters ($1/n$) and K_F, Temkin parameters (B and K_T) for adsorption of MO onto WB-AC at Equilibrium (0.1 mg L^{-1}).

Langmuir model			Freundlich model			Temkin model		
q_{max}	K_L	R^2	$1/n$	K_F	R^2	B	K_T	R^2
555	0.0119	0.6737	0.3078	0.7652	0.8223	5.43	3.6056	0.5659

ChemPlusChem

Research Article
doi.org/10.1002/cplu.202300373

Chemistry Europe
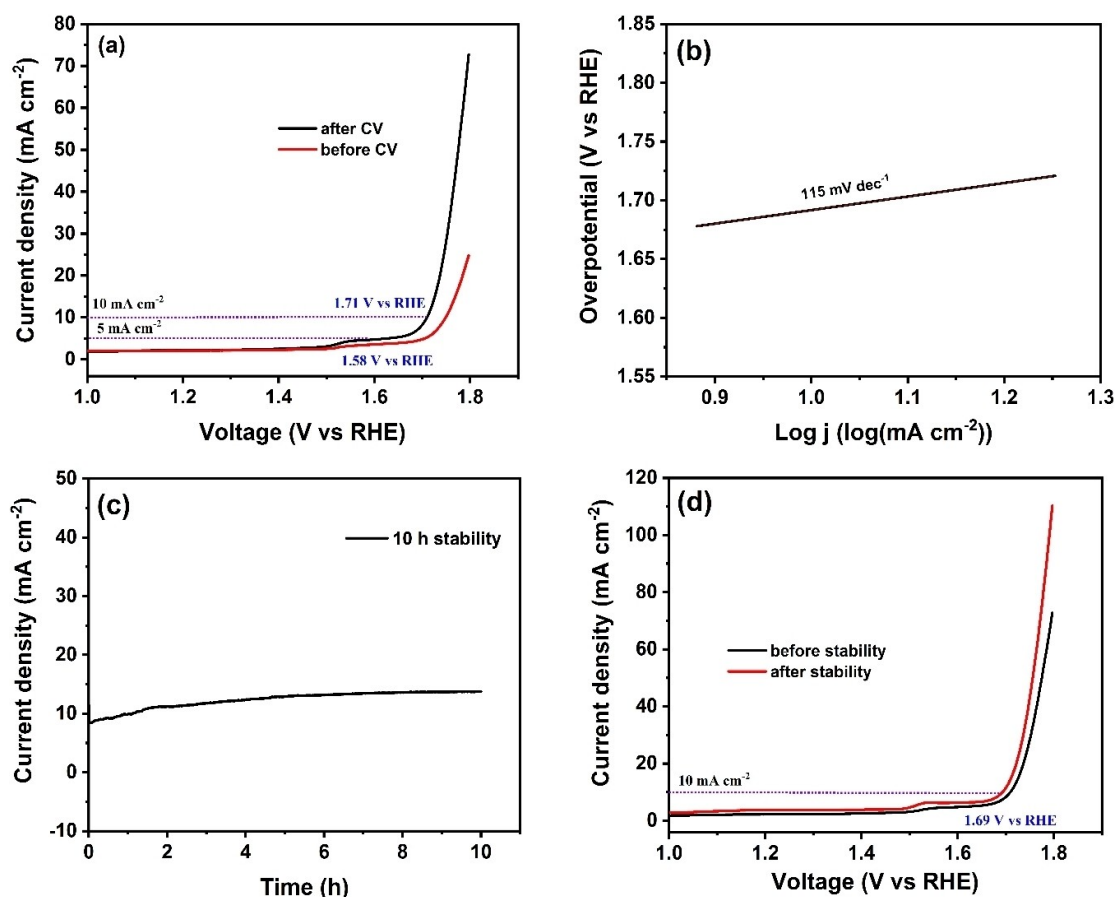European Chemical
Societies Publishing

Figure 7. Electrocatalytic OER performance of WB-AC in 1 M KOH (a) LSV curve before and after cycling, (b) Tafel slope, (c) Chronoamperometric stability study at current density of 10 mA cm^{-2}, (d) LSV curve before and after stability

interpretation on the mechanism of the OER.[65] The tafel slope is determined by fitting linear portions of low overpotential values of the LSV data to the Tafel Eq. S12. The tafel plot of WB-AC is shown in Figure 7b. A small tafel slope indicates a greatly enhanced OER rate at a low overpotential. A tafel slope of about 115 mV dec^{-1} was obtained for WB-AC, indicating the higher electrocatalytic activity of the material. A small value of slope suggests its favorable reaction kinetics and excellent i-V response for an applied low overpotential value.

The electrochemical impedance spectroscopic (EIS) measurements were detailed in order to understand the faster electron transfer kinetics before and after CV continuous cycles. The charge transfer resistance (Rct) was enormously decreased to 413 Ω from 231 Ω after 1000 continuous CV cycles, significantly improving the OER performance. The enhanced OER activity of the WB-AC is attributed to decreased charge-transfer resistance (Figure S10b). The long-term stability of the material is an important parameter to be considered for an OER activity.[64] Then the long-term stability was initiated by chronoamperometric (i-t) method with a current density input of 10 mA cm^{-2} for about 10 h (Figure 7c). The WB-AC exhibited relatively good stability, with a slight increase in current density during the measurements, as a result of its better activity for OER, which is in agreement with the data obtained by other

electrochemical methods. There is no significant change in LSV before and after the 10 h stability test, revealing that the WB-AC has high stability towards OER under 1 M KOH as shown in Figure 7d.

Impressed with superior OER activity, the WB-AC electrode was also explored for HER using 1.0 M KOH. It was noticed that the WB-AC also exhibited better HER activity in basic-medium. Figure 8a shows LSV curves with iR compensation performed at ~0.0 to −0.8 V vs. RHE. The WB-AC electrode delivered low overpotentials of 57, 82 and 101 mV at 10, 20 and 30 mA cm^{-2}, respectively. The HER mechanism of WB-AC is further characterized by Tafel plots on the basis of the LSV curve. The HER kinetics observed at the slope of 82.6 mV dec^{-1} corresponds to the Volmer-Heyrovsky mechanism, where the H$_2$ adsorption and desorption arise sequentially in a two-step process. From the Tafel slope measurements, it can be concluded that the WB-AC shows a lower tafel slope, indicating high HER activity (Figure 8b).

As shown in Figure 8c the stability curve with a current density of 10 mA cm^{-2} for about 10 h, shows short decrement and recovery in the response. It was seen that the performance was due to the periodic accumulation and discharge of H$_2$ bubbles from the surface of the WB-AC electrode. LSV graphs were documented before and after long-term stability, as

ChemPlusChem

Research Article
doi.org/10.1002/cplu.202300373

Chemistry Europe
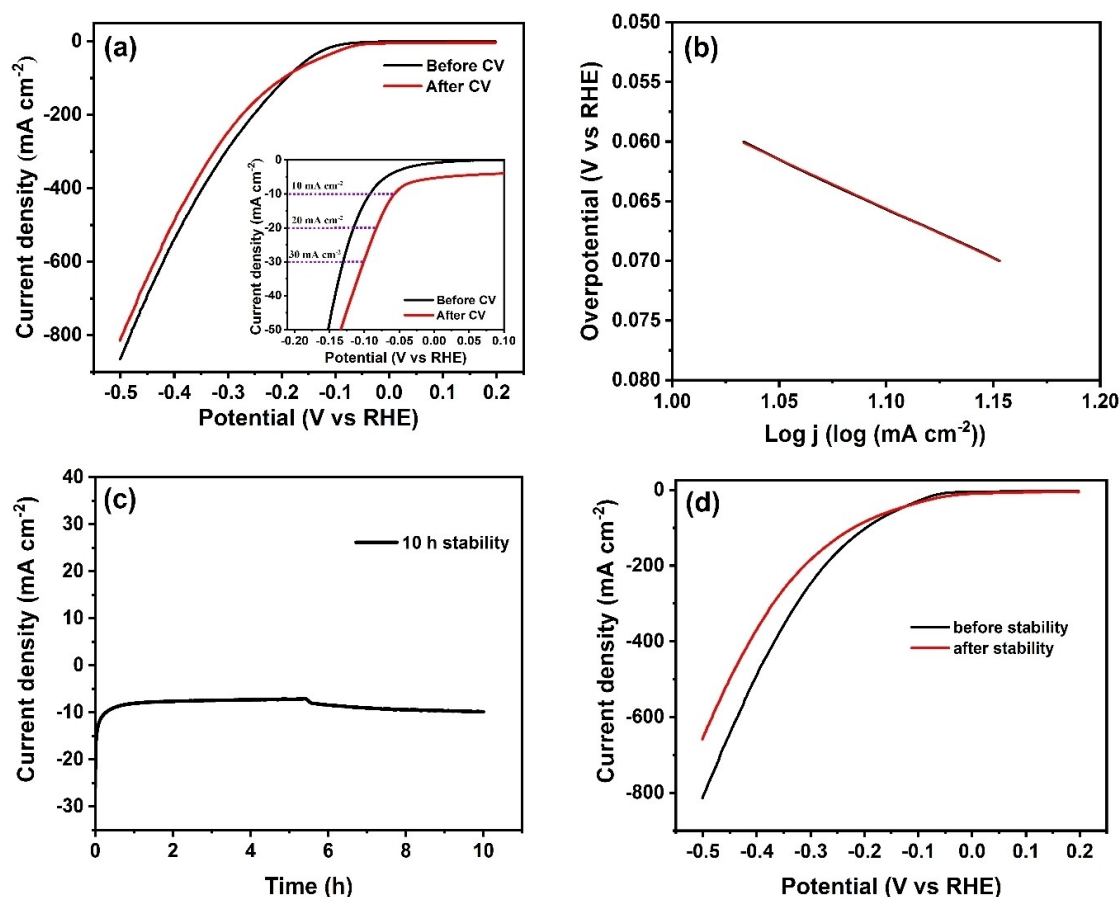European Chemical
Societies Publishing

Figure 8. Electrocatalytic HER performance of WB-AC in 1 M KOH (a) LSV curve before and after cycling, (b) Tafel slope, (c) Chronoamperometric stability study at current density of 10 mA cm^2, (d) LSV curve before and after stability

shown in Figure 8d. It can be seen that there are no significant changes observed from the LSV, indicating the good stability of the WB-AC. From the electrochemical studies, it was observed that WB-AC possesses high HER activity, with faster reaction kinetics and good long-term stability.

Additionally, noticeable pseudocapacitive performance is supplemented by enhanced electrocatalytic activity; high pseudocapacitance confirms the existence of a number of active sites that can be responsible for the sorption process of O_2, OH^-, H^+ present on the surface of catalyst.[65] In the present work, no obvious change in the capacitance nature was observed, while cycling improved the electrochemical activity of WB-AC. In addition, the high surface area and the abundant hierarchical pores behave like a connected bridge for mass and charge transport between electrolyte, active surface and conductive substrate, leading to better OER and HER electrochemical activity. In particular, the macropores can speed up mass transportation and penetrate electrolytes, while hierarchical pores can assist in the well-organized transfer of reactants, decreasing the diffusion rate and boosting the reaction efficiency.[66] Meanwhile, an oxygen containing functional group on the surface of C provides the catalytic core and can play dual-nature, making the material slightly hydrophilic by interacting with water and serving as an active core to accelerate

the dissociation of water molecules. By facilitating the C atoms to adsorb OH^-, H^+ or H_2O, the electron transfer can be accelerated and the OER/HER is promoted ultimately.[67] This order of action was further confirmed by the observation of higher current at low OER and HER potential. All these electrochemical studies prove that the WB-AC has superior electrocatalytic activity towards OER and HER with excellent kinetics and robust stability, which can be used as low-cost metal-free catalyst for water electrolysis.

Conclusions

In summary, the ordered hierarchical porous AC is successfully prepared by chemical carbonization followed by a physical activation approach from easily available wheat-bran agrowaste, considering the best utilization of waste. Our results conclude that the N_2 activation significantly enhances the SSA from 246 m^{2}g^{-1} to 757 m^{2}g^{-1} and pore volume from 0.1237 cm^{3}g^{-1} to 0.3696 cm^{3}g^{-1}, respectively. The obtained HPAC (WB-AC) exhibits a higher CO_2 capture capacity (2.47 mmol g^{-1}) along with high CO_2/N_2 selectivity (40.10). In addition, WB-AC was found to be a highly efficient adsorbent for faster removal of MO dye with 555 mg g^{-1} adsorption

ChemPlusChem

Research Article
doi.org/10.1002/cplu.202300373

Chemistry Europe
European Chemical
Societies Publishing

capacity. Moreover, WB-AC demonstrated a good OER activity with a less positive onset potential of 1.58 V, a low overpotential of 0.35 V at 5 mA cm^{-2} current density, and a small Tafel slope of 115 mV dec^{-1}. The WB-AC also exhibited high electrocatalytic HER activity with a low overpotential of 57 mV at 10 mA cm^{-2}, and a small Tafel slope of 82.6 mV dec^{-1}. The WB-AC has superior electrochemical activity towards OER and HER with excellent kinetics and robust stability. Owing to these advantages, we conclude that the reported hierarchical porous WB-AC will be utilized as a promising and sustainable adsorbent as well as metal-free catalyst for potential CO_2 capture, environmental remediation and water electrolysis.

Materials and Methods

Synthesis of WB derived activated carbon (WB-AC)

The WB-AC was prepared by acid carbonization followed by N_2 activation. The WB used in this work was collected after sieving the wheat flour and screened to obtain a 2–5 mm mesh powder. The WB powder was then soaked in H_2SO_4 (mass ratio of 1:1) for 24 h at room temperature with intermittent stirring to ensure complete carbonization.[68] The obtained carbon was repetitively washed with DI to eliminate excess acid and vacuum dried at 373 K obtained material termed raw carbon (WB-RC). Finally, the fine powder of WB-RC was activated under N_2 flow at 773 K for 2 h with a heating rate of 20 K per minute in a tube furnace. The resulting product, WB-AC, was ground to a smaller size and stored in a desiccator for further study. H_2SO_4 (AR grade, Fisher Scientific, India) and MO dye (Spectrochem Pvt. Ltd. India) was used.

Characterization

To get insights into structural and surface details of synthesized WB-RC and WB-AC PXRD (Philips X-ray diffractometer, Ni Cu Kα radiation) and FTIR (FTIR-4600, Jasco, Japan model) were performed, respectively. The morphology was revealed using field emission SEM (FESEM, JEOL, JSM-6360). The elemental composition was recorded using Elemental Analyzer (Thermo, Finnigan). In-depth surface functionality was elaborated using X-ray photoelectron spectroscopy (Shimadzu ESCA 3400 instrument). The surface area and pore volume were determined from N_2 adsorption-desorption isotherms using a BET analyzer (Bellsorp mini II, Japan). The Barret-Joyner-Holanda (BJH) method was applied to determine pore size distribution.

CO_2 adsorption studies

The WB-RC and WB-AC samples were degassed under a vacuum at 573 K for 5 h to eliminate the guest molecules from the carbon pores. The adsorption experiments were conducted at 288, 298 and 308 K temperatures (1 atm) using a gas adsorption analyzer (Bellsorp mini II). The dead volume was determined using helium gas. In order to accompany the CO_2 adsorption work, the isosteric heat of adsorption was determined based on the Clausius-Clapeyron equation (Eq. S1) using CO_2 adsorption isotherms at different temperatures. The Single-site and Dual-site Langmuir models were explored to determine the adsorption correlation (Eq. S2 and Eq. S3). In addition, Henry's Law (Eq. S4–S6) was employed to predict CO_2/N_2 selectivity.

Dye removal studies

The dye removal efficiency of WB-AC was determined using batch equilibrium adsorption experiments. The experiments were carried out in a succession of solutions with 0.1 g WB-AC and 50 mL MO dye solution in the 10–200 mg L^{-1} concentration range. The dye and WB-AC were thoroughly mixed with shaking on an orbital shaker at 200 rpm. The 2 mL dye solution segments were collected at incremental time intervals, and the filter membrane (0.22 μm) was used to separate WB-AC from the dye solution. The absorbance of the solution was measured at 464 nm with a UV-vis spectrophotometer (UV-3600, Lab India). The % dye removal (Eq. S7) and adsorption kinetics was determined from the 10 mg L^{-1} MO dye experiment, while the equilibrium adsorption capacity (q_e) of the WB-AC for MO was determined using Eq. S8.

Electrochemical studies

All the electrochemical measurements were investigated using CH-USA electrochemical workstation in three-electrode set-up, consisting of a Ni foam working electrode, graphene rod as a counter and saturated calomel as a reference electrode. For all the measurements, the potentials were converted to reversible hydrogen electrode (vs RHE). The WB-AC ink was prepared by the dispersion of 4.0 mg of the sample in 796 μL of water, 200 μL of isopropyl alcohol and 40 μL of Nafion. The mixture was sonicated for 20 min. Then, 4.0 μL of the above solution was drop cast onto the surface of Ni foam. The as-prepared electrode was dried at room temperature overnight and further used to study the electrochemical activity of the material.

Abbreviations

WB- Wheat bran; **RC**- Raw carbon; **AC**- Activated carbon; **MO**- Methyl orange; **PSD**- Pore size distribution; **PACs**- Porous activated carbons; **SSA**- Specific surface area; **DI water**- Deionized water; **Qst**- Isosteric heat of adsorption, **OER**-Oxygen evolution reaction, **HER**-Hydrogen evolution reaction, **MP**- Micropore volume, **LSV**-Linear sweep voltammogram, **EIS**- Electrochemical impedance spectroscopic, **CV**–Cyclic voltammetry

Supporting Information

Acknowledgements

Conflict of Interests

Authors declare that there are no any competing interests.

Data Availability Statement

Data sharing is not applicable to this article as no new data were created or analyzed in this study.

[1] M. Ades, R. Adler, R. Allan, R. Allan, J. Anderson, A. Argüez, C. Arosio, J. Augustine, C. Azorin-Molina, J. Barichivich, *Bull. Am. Meteorol. Soc.* **2020**, *101*, S9–S128.

[2] P. K. Sadh, S. Duhan, J. S. Duhan, *Bioresour. Bioprocess.* **2018**, *5*, 1–15.

[3] W. Liang, M. Yang, *Sustain. Comput. Inform. Syst.* **2019**, *21*, 1–9.

[4] J. Sun, J. Wang, T. Wang, T. Zhang, *Manag. Environ. Qual. Int. J.* **2019**, *30*, 483–494.

[5] M. Wang, A. S. Joel, C. Ramshaw, D. Eimer, N. M. Musa, *Appl. Energy* **2015**, *158*, 275–291.

[6] A. Inyinbor Adejumoke, in *Water Chall. Urban. World* (Ed.: Adebesin Babatunde O.), Intech Open, Rijeka, **2018**, p. Ch. 3.

[7] P. R. Rout, T. C. Zhang, P. Bhunia, R. Y. Surampalli, *Sci. Total Environ.* **2021**, *753*, 141990.

[8] F. M. D. Chequer, G. A. R. de Oliveira, E. R. A. Ferraz, J. C. Cardoso, M. V. B. Zanoni, D. P. de Oliveira, *Textile Dyes: Dyeing Process and Environmental Impact*, IntechOpen, **2013**.

[9] M. Berradi, R. Hsissou, M. Khudhair, M. Assouag, O. Cherkaoui, A. El Bachiri, A. El Harfi, *Heliyon* **2019**, *5*, e02711.

[10] S. El Harfi, A. El Harfi, *Appl. J. Environ. Eng. Sci.* **2017**, *3*, 00000–00003.

[11] K.-T. Chung, *J. Environ. Sci. Health Part C* **2016**, *34*, 233–261.

[12] Md. M. Haque, Md. A. Haque, M. K. Mosharaf, P. K. Marcus, *Saudi J. Biol. Sci.* **2021**, *28*, 793–804.

[13] S. Rattanapan, J. Srikram, P. Kongsune, *Energy Procedia* **2017**, *138*, 949–954.

[14] P. Gregory, *Dyes Pigm.* **1986**, *7*, 45–56.

[15] N. Bolong, A. F. Ismail, M. R. Salim, T. Matsuura, *Desalination* **2009**, *239*, 229–246.

[16] K. O. Iwuozor, J. O. Ighalo, E. C. Emenike, L. A. Ogunfowora, C. A. Igwegbe, *Curr. Res. Green Sustain. Chem.* **2021**, *4*, 100179.

[17] L. Wu, X. Liu, G. Lv, R. Zhu, L. Tian, M. Liu, Y. Li, W. Rao, T. Liu, L. Liao, *Sci. Rep.* **2021**, *11*, 10640.

[18] P. Manasa, S. Sambasivam, F. Ran, *J. Energy Storage* **2022**, *54*, 105290.

[19] M. A. Yahya, Z. Al-Qodah, C. Z. Ngah, *Renewable Sustainable Energy Rev.* **2015**, *46*, 218–235.

[20] R. Manikandan, S. Sadhasivam, S. Lee, Seung-Cheol Chang, K. Ashok Kumar, C. Bathula, V. Gopalan Sree, D. Young Kim, S. Sekar, *J. Mol. Liq.* **2023**, *375*, 121338.

[21] T. Pepè Sciarria, M. A. C. de Oliveira, B. Mecheri, A. D'Epifanio, J. L. Goldfarb, F. Adani, *J. Power Sources* **2020**, *462*, 228183.

[22] B. J. Riley, S. Chong, J. Schmid, J. Marcial, E. T. Nienhuis, M. K. Bera, S. Lee, N. L. Canfield, S. Kim, M. A. Derewinski, R. K. Motkuri, *ACS Appl. Mater. Interfaces* **2022**, *14*, 18439–18452.

[23] L. Estevez, D. Barpaga, J. Zheng, S. Sabale, R. L. Patel, J.-G. Zhang, B. P. McGrail, R. K. Motkuri, *Ind. Eng. Chem. Res.* **2018**, *57*, 1262–1268.

[24] D. Barpaga, J. Zheng, B. P. McGrail, R. K. Motkuri, *Acc. Chem. Res.* **2021**, *55*, 649–659.

[25] J. Zheng, M. Wahiduzzaman, D. Barpaga, B. A. Trump, O. Y. Gutiérrez, P. Thallapally, S. Ma, B. P. McGrail, G. Maurin, R. K. Motkuri, *Angew. Chem. Int. Ed.* **2021**, *60*, 18037–18043.

[26] J. Zheng, D. Barpaga, B. A. Trump, M. Shetty, Y. Fan, P. Bhattacharya, J. J. Jenks, C. Y. Su, C. M. Brown, G. Maurin, B. P. McGrail, R. K. Motkuri, *J. Am. Chem. Soc.* **2020**, *142*, 3002–3012.

[27] A. Koli, A. K. Battu, R. K. Motkuri, S. Sabale, *Biomass Convers. Biorefinery* **2022**, DOI 10.1007/s13399-022-03067-y.

[28] P. Kaur, G. Verma, S. S. Sekhon, *Prog. Mater. Sci.* **2019**, *102*, 1–71.

[29] G. Mezohegyi, F. P. van der Zee, J. Font, A. Fortuny, A. Fabregat, *J. Environ. Manage.* **2012**, *102*, 148–164.

[30] A. Mukherjee, J. A. Okolie, A. Abdelrasoul, C. Niu, A. K. Dalai, *J. Environ. Sci.* **2019**, *83*, 46–63.

[31] J. Bedia, M. Peñas-Garzón, A. Gómez-Avilés, J. J. Rodriguez, C. Belver, *C* **2018**, *4*, 63.

[32] N. Mohamad Nor, L. C. Lau, K. T. Lee, A. R. Mohamed, *J. Environ. Chem. Eng.* **2013**, *1*, 658–666.

[33] A. Katileviciute, G. Plakys, A. Budreviciute, K. Onder, S. Damiati, R. Kodzius, *Biomol. Eng.* **2019**, *9*, 887.

[34] F. Björnerbäck, N. Hedin, *ACS Sustainable Chem. Eng.* **2019**, *7*, 1018–1027.

[35] A. Koli, R. Dhabbe, J. Shen, R. K. Motkuri, S. Sabale, *Biomass Convers. Biorefinery* **2023**, DOI 10.1007/s13399-023-04140-w.

[36] S. Balou, S. E. Babak, A. Priye, *ACS Appl. Mater. Interfaces* **2020**, *12*, 42711–42722.

[37] H. A. Rahman, S. X. Chin, *Sains Malays.* **2019**, *48*, 385–391.

[38] I. Bautista-Toledo, M. A. Ferro-García, J. Rivera-Utrilla, C. Moreno-Castilla, F. J. Vegas Fernández, *Environ. Sci. Technol.* **2005**, *39*, 6246–6250.

[39] P. D. Tomke, V. K. Rathod, *Int. J. Biol. Macromol.* **2018**, *117*, 366–376.

[40] J. Coates, in *Encycl. Anal. Chem.*, John Wiley & Sons, Ltd, **2006**.

[41] M. Karnan, K. Subramani, N. Sudhan, N. Ilayaraja, M. Sathish, *ACS Appl. Mater. Interfaces* **2016**, *8*, 35191–35202.

[42] X. Wang, L. Xiong, L. Li, J. Zhong, *Greenh. Gases Sci. Technol.* **2020**, *10*, 461–471.

[43] B. Yuan, X. Wu, Y. Chen, J. Huang, H. Luo, S. Deng, *Environ. Sci. Technol.* **2013**, *47*, 5474–5480.

[44] J. Wang, X. Guo, *Chemosphere* **2020**, *258*, 127279.

[45] L. Xiong, X.-F. Wang, L. Li, J. Jin, Y.-G. Zhang, S.-L. Song, R.-P. Liu, *Energy Fuels* **2019**, *33*, 12558–12567.

[46] J. Wang, Q. Liu, *Nanoscale* **2014**, *6*, 4148–4156.

[47] D. Lennon, D. T. Lundie, S. D. Jackson, G. J. Kelly, S. F. Parker, *Langmuir* **2002**, *18*, 4667–4673.

[48] J. Sodtipinta, T. Amornsakchai, P. Pakawatpanurut, *Adv. Nat. Sci. Nanosci. Nanotechnol.* **2017**, *8*, 035017.

[49] X. Li, S. Bai, Z. Zhu, J. Sun, X. Jin, X. Wu, J. Liu, *Langmuir* **2017**, *33*, 1248–1255.

[50] M. Shi, X. Wang, M. Shao, L. Lu, H. Ullah, H. Zheng, F. Li, *Front. Environ. Sci. Eng.* **2022**, *17*, 5.

[51] J. Cai, J. Qi, C. Yang, X. Zhao, *ACS Appl. Mater. Interfaces* **2014**, *6*, 3703–3711.

[52] M. Balsamo, A. Silvestre-Albero, J. Silvestre-Albero, A. Erto, F. Rodriguez-Reinoso, A. Lancia, *Langmuir* **2014**, *30*, 5840–5848.

[53] E. Perez-Botella, R. Martinez-Franco, N. González-Camuñas, A. Cantin, M. Palomino, M. Moliner, S. Valencia, F. Rey, *Front. Chem.* **2020**, *8*.

[54] P. M. Mathias, R. Kumar, J. D. Moyer, J. M. Schork, S. R. Srinivasan, S. R. Auvil, O. Talu, *Ind. Eng. Chem. Res.* **1996**, *35*, 2477–2483.

[55] T. Chen, S. Deng, B. Wang, J. Huang, Y. Wang, G. Yu, *RSC Adv.* **2015**, *5*, 48323–48330.

[56] L. Shao, Y. Li, J. Huang, Y.-N. Liu, *Ind. Eng. Chem. Res.* **2018**, *57*, 2856–2865.

[57] D. Hulicova-Jurcakova, M. Seredych, G. Q. Lu, T. J. Bandosz, *Adv. Funct. Mater.* **2009**, *19*, 438–447.

ChemPlusChem

Research Article
doi.org/10.1002/cplu.202300373

Chemistry Europe
European Chemical
Societies Publishing

[58] A. M. Aljeboree, A. N. Alshirifi, A. F. Alkaim, *Arab. J. Chem.* **2017**, *10*, S3381–S3393.

[59] E. Sharifpour, E. Alipanahpour Dil, A. Asfaram, M. Ghaedi, A. Goudarzi, *Appl. Organomet. Chem.* **2019**, *33*, e4768.

[60] A. S. Sartape, A. M. Mandhare, V. V. Jadhav, P. D. Raut, M. A. Anuse, S. S. Kolekar, *Arab. J. Chem.* **2017**, *10*, S3229–S3238.

[61] R. Zambare, X. Song, S. Bhuvana, J. S. Antony Prince, P. Nemade, *ACS Sustainable Chem. Eng.* **2017**, *5*, 6026–6035.

[62] N. Grishkewich, N. Mohammed, S. Wei, M. Vasudev, Z. Shi, R. M. Berry, K. C. Tam, *Ind. Eng. Chem. Res.* **2020**, *59*, 20854–20865.

[63] Y.-T. Pi, X.-Y. Xing, L.-M. Lu, Z.-B. He, T.-Z. Ren, *RSC Adv.* **2016**, *6*, 102422–102427.

[64] N. Prabu, T. Kesavan, G. Maduraiveeran, M. Sasidharan, *Int. J. Hydrogen Energy* **2019**, *44*, 19995–20006.

[65] K. R. A. Saravanan, N. Prabu, M. Sasidharan, G. Maduraiveeran, *Appl. Surf. Sci.* **2019**, *489*, 725–733.

[66] Y. Orooji, N. Han, Z. Nezafat, N. Shafiei, Z. Shen, M. Nasrollahzadeh, H. Karimi-Maleh, R. Luque, A. Bokhari, J. J. Klemeš, *J. Cleaner Prod.* **2022**, *347*, 131220.

[67] D. J. Tarimo, K. O. Oyedotun, A. A. Mirghni, N. F. Sylla, N. Manyala, *Electrochim. Acta* **2020**, *353*, 136498.

[68] T. Khan, M. H. Isa, M. R. U. Mustafa, H. Yeek-Chia, L. Baloo, T. S. B. Abd Manan, M. O. Saeed, *RSC Adv.* **2016**, *6*, 56365–56374.

[69] K. Li, S. Tian, J. Jiang, J. Wang, X. Chen, F. Yan, *J. Mater. Chem. A* **2016**, *4*, 5223–5234.

[70] X.-F. Wang, L. Xiong, J.-J. Zhong, L. Jin, J.-L. Yan, B. Mu, Y.-G. Zhang, S.-L. Song, *Ind. Eng. Chem. Res.* **2020**, *59*, 18106–18114.

[71] X. Ma, Y. Li, M. Cao, C. Hu, *J. Mater. Chem. A* **2014**, *2*, 4819–4826.

[72] A. S. Mestre, C. Freire, J. Pires, A. P. Carvalho, M. L. Pinto, *J. Mater. Chem. A* **2014**, *2*, 15337–15344.

[73] Z. Rouzitalab, D. Mohammady Maklavany, A. Rashidi, S. Jafarinejad, *J. Environ. Chem. Eng.* **2018**, *6*, 6653–6663.

[74] Z. Geng, Q. Xiao, H. Lv, B. Li, H. Wu, Y. Lu, C. Zhang, *Sci. Rep.* **2016**, *6*, 30049.

[75] M. Rana, K. Subramani, M. Sathish, U. K. Gautam, *Carbon* **2017**, *114*, 679–689.

[76] L. Yue, Q. Xia, L. Wang, L. Wang, H. DaCosta, J. Yang, X. Hu, *J. Colloid Interface Sci.* **2018**, *511*, 259–267.

[77] V. da Silva Lacerda, J. B. López-Sotelo, A. Correa-Guimarães, S. Hernández-Navarro, M. Sánchez-Báscones, L. M. Navas-Gracia, P. Martín-Ramos, J. Martín-Gil, *J. Environ. Manage.* **2015**, *155*, 67–76.

[78] K. Geetha, V. Nanjan, D. S. Karthikeyan, S. P. S. Shabudeen, *Carbon – Sci. Tech.* **2014**, *6*, 395–406.

[79] W. Qu, T. Yuan, G. Yin, S. Xu, Q. Zhang, H. Su, *Fuel* **2019**, *249*, 45–53.

[80] P. V. Thitame, S. R. Shukla, *Chem. Eng. Commun.* **2016**, *203*, 791–800.

[81] O. Baytar, Ö. Şahin, C. Saka, *Appl. Therm. Eng.* **2018**, *138*, 542–551.

[82] M. Ghasemi, S. Mashhadi, H. Javadian, T. Saleh, V. Gupta, *Desalination Water Treat.* **2016**, *57*, DOI 10.1080/19443994.2015.1119737.

[83] A. H. Jawad, R. A. Rashid, M. A. M. Ishak, L. D. Wilson, *Desalination water Treat.* **2016**, *57*, 25194–25206.

[84] V. C. Hoang, V. G. Gomes, K. N. Dinh, *Electrochim. Acta* **2019**, *314*, 49–60.

[85] Z. Yang, C. Yan, M. Xiang, Y. Shi, M. Ding, J. Hui, *Int. J. Energy Res.* **2021**, *45*, 8474–8483.

[86] Z. Liu, Q. Zhou, B. Zhao, S. Li, Y. Xiong, W. Xu, *Fuel* **2020**, *280*, 118567.

[87] K. Pandey, H. K. Jeong, *Chem. Phys. Impact* **2023**, *6*, 100175.

[88] S. Sekar, A. T. Aqueel Ahmed, S. M. Pawar, Y. Lee, H. Im, D. Y. Kim, S. Lee, *Appl. Surf. Sci.* **2020**, *508*, 145127.

[89] S. D. Raut, N. M. Shinde, Y. T. Nakate, B. G. Ghule, S. K. Gore, S. F. Shaikh, J. J. Pak, A. M. Al-Enizi, R. S. Mane, *ACS Omega* **2021**, *6*, 12623–12630.

[90] C. Xia, S. Surendran, S. Ji, D. Kim, Y. Chae, J. Kim, M. Je, M.-K. Han, W.-S. Choe, C. H. Choi, H. Choi, J. K. Kim, U. Sim, *Carbon Energy* **2022**, *4*, 491–505.

ORIGINAL ARTICLE

The role of composition and porosity of MOF derived Cu-embedded carbon electrocatalyst for oxygen evolution reaction

Mahesh Burud[1] · Amruta Koli[2] · Akshata Pattanshetti[2] · Prathamesh Chougale[2] · Rohant Dhabbe[2] · Vijay Chavan[3] · Deok-kee Kim[3] · Amit Supale[1] · Sandip Sabale[2]

Abstract

Oxygen evolution reaction (OER) plays a vital role in the field of water splitting, which has a promising way of achieving high efficiency and clean energy. However, a large overpotential and sluggish kinetics limit the water splitting efficiency. Thus, development of effective electrocatalyst is a key point to make OER more practicable. In this communication, we account a metal–organic framework (MOF) pyrolization path for derived Cu-embedded porous carbon materials as electrocatalyst for efficient and superior OER application in an alkaline condition. The prominent effect of pyrolysis was observed on the porosity as well as Cu content which predominates its electrocatalytic properties. The rise in pyrolysis temperature decreases surface area (SSA) due to more contribution of macroporosity. The hybrid Cu_2O/Cu connected porous carbon form of the CuBTC C600 provides large channels for rapid electron transfer and beneficial for electrolyte penetration which enhances the catalytic property results in to a low overpotential of 310 mV @10 mA/cm^2 and Tafel slope (80 mV dec^{-1}), and exceptional long-term stability as compared to CuBTC and rest materials. The role of porosity and consortium effect of Cu NPs and Cu_2O along with effect of pyrolysis was studied and discussed.

Keywords Metal organic frameworks · CuBTC · Oxygen evolution reactions · Electrocatalyst

1 Introduction

Worldwide burgeoning demand for green and renewable energy caused by the scarcity of fossil fuels and increasing grievous environmental issues has lead to urgent need to develop clean and sustainable energy [1]. To overcome this global issue, the necessity to generate green and clean energy, electrocatalytically water splitting is the highly efficient, and eco-friendly technologies, it is a promising technique for conversion systems [2]. The water electrolyzer is composed of two half-cell reactions including, hydrogen evolution reaction (HER) and oxygen evolution reaction (OER) at the cathode and anode respectively, which furnishes an origin of clean and renewable energy. Among both, OER shows very crucial reaction of water electrolysis (4 $OH^- \rightarrow O_2 + 2\ H_2O + 4\ e^-$ in alkaline electrolytes) and is a sluggish kinetics due to the four-electron transfer process for the production of O_2 and requires a large overpotential for driving the anodic OER [3]. To improve the kinetics of OER, many efforts have been dedicated to develop effectual electrocatalysts. Traditionally, OER is catalyzed by precious noble metals, such as IrO_2, and RuO_2 demonstrate very high catalytic activity and stability, but their scarceness, expensiveness, and their less abundance on the earth's crust hinder their large-scale applications [4]. Besides researchers also reported a potential use of vanadium, activated carbons, ferrites, metal oxides, and hydroxides for the HER/OER applications [1–3, 5]. However, to design and synthesize a more efficient, less expensive, and environmentally benign non-noble metal-based electrocatalyst is indispensable to diminishing energy consumption.

✉ Amit Supale
amit.supale@bharatividyapeeth.edu

✉ Sandip Sabale
srsabale@gmail.com

1 Department of Chemistry, Bharati Vidyapeeth's Dr. Patangrao Kadam Mahavidyalaya, (Shivaji University Kolhapur), Sangli 416416, MS, India

2 Department of Chemistry, Jaysingpur College, Jaysingpur 416101, MS, India

3 Department of Electrical Engineering and Convergence Engineering for Intelligent Drone, Sejong University, Seoul 05006, Republic of Korea

Scheme 1 Schematic illustration of synthesis of CuBTC derived Cu-embedded carbon electrocatalyst
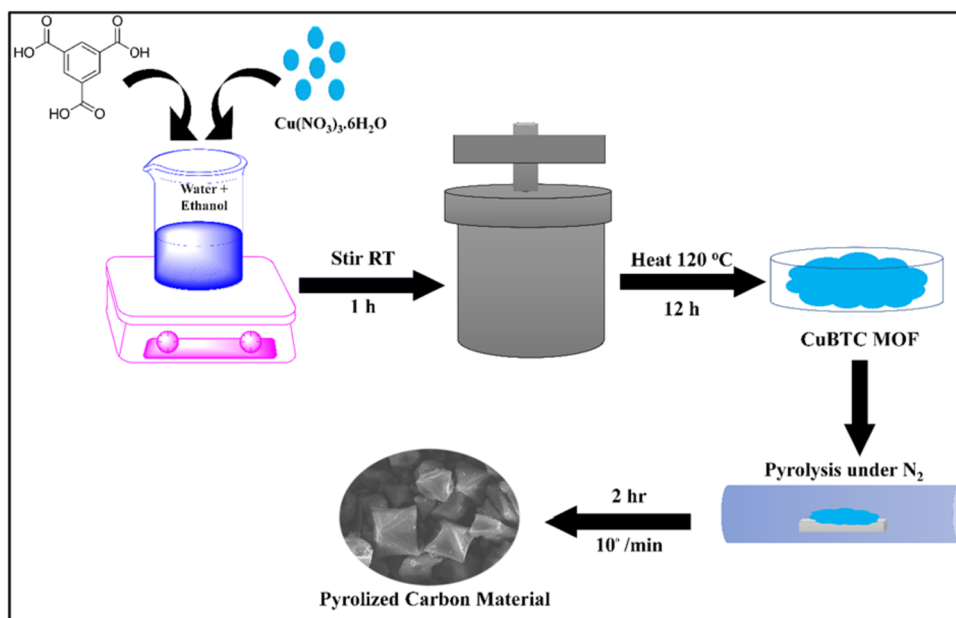
Transition metal-based oxide, hydroxides, metal phosphide, and carbonaceous nanomaterials exhibit optimistic electrocatalytic performance for OER. Recently extensive research has been made to find transition metal-based nanomaterials owing to the fact that low cost, abundant in nature, and eco-friendly nature [6]. A MOF is a promising material in electrochemistry, having more significant attention as a material for catalysis cause of their advantages such as flexible pore size, and large surface area [7–9]. The poor conductivity of MOF materials limits electrochemical performance, substantial efforts have been made to develop innovative pathways to enhance conductivity and improve MOF materials electrochemical performance [10]. To reduce this problem, MOF nanomaterials doping with heteroatoms, coupling with conductive carbonaceous nanomaterials, calcination, and pyrolysis, is an effective path to improve the electrocatalytic performance [11–13]. Therefore, it is essential to develop a catalytic material with more abundance in the earth's crust, easily available, cheap, functioning at low overpotential, and attains excellent catalytic activity with long term stability towards OER. The appropriate materials (heteroatoms and conductive materials) can be used, which modifies the catalytic activity. The transition metal-based MOFs nanomaterials exhibit excellent electrocatalytic performance as an electrocatalyst, and many research communities have made more efforts to fabricate superior nanomaterials for OER applications. Owing to their excellent intrinsic performance, MOFs used as templates [14] for producing MOF-derived metal oxides, metal hydroxides, porous carbon, and their hybrids material by direct calcination and pyrolysis [15]. There are various methods known to synthesize porous carbons [16] as well as carbon-supported [10] electrocatalysts including calcination and pyrolysis. In

pyrolysis, MOF (used as a template) is simply heated at higher temperature to attain metal embedded porous carbon material. This type of MOF-derived carbon supported nanoparticles provides metal dispersion and possesses good surface properties that make them superior electrocatalyst [17].

In the present work, the Cu-BTC MOF is synthesized using the reported method [18] followed by pyrolyzed at different temperatures under N_2 gas (Scheme 1). The structural, compositional, and morphological changes were determined for their effect on electrocatalysis for OER application. Copper as well as porous carbon plays a crucial role in the OER which attracted us to synthesize the Cu-BTC and its carbonaceous materials. These results provide a good opportunity to develop carbon-embedded Cu-based electrocatalysts by varying pyrolysis temperatures. The study investigated the role of the porosity of carbon material derived from CuBTC MOF, the impact of pyrolysis, and the combined effect of Cu NPs and Cu_2O on the catalytic properties of the activated carbons. This research likely sheds light on the potent applications of these materials in electrocatalysis along with the role of meso-micro pore structure. The carbonization strategy under the N_2 atmosphere is found to be beneficial in improving the structural morphology, and porosity for energy applications as well as a pathway for the researchers.

2 Experimental section

2.1 Materials and methods

Trimesic acid (H_3BTC; CAS 554–95-0) was obtained from Sigma Aldrich, India, and copper (II) nitrate trihydrate,

$Cu(NO_3)_2.3H_2O$ was purchased from Thomas Baker, India. Ethanol (C_2H_5OH; CAS 64–17-5) was purchased as an analytical grade, and distilled water was used throughout this work. All chemicals are used directly without further purification.

2.2 Synthesis of CuBTC MOF and its derived Cu-embedded carbons

The trimesic acid 0.42 g (2.0 mmol) and $Cu(NO_3)_2.3H_2O$, 0.87 g (3.6 mmol) was dissolved in 24 mL ethanol/water mixture with constant stirring for 1 h at room temperature. The obtained blue solution was transferred into a 100 mL Teflon-lined autoclave and heated at 120℃ for 12 h followed by cooling at room temperature naturally. The obtained CuBTC MOF was further subjected for washing and drying.

Thereafter, the CuBTC powder was placed in an electric tubular furnace and heated at different temperatures viz. 400, 600, and 800℃ for 2 h under a nitrogen atmosphere with a heating rate of 10℃/min and obtained black powder were designated as CuBTC C400, CuBTC C600, and CuBTC C800 respectively (Scheme 1).

2.3 Materials characterization

X-ray powder diffraction (XRD) was utilized to analyse the crystal structure of the prepared sample material. XRD analysis was performed on Bruker, AXS D8-Advance, using Cu Kα radiation ($\lambda = 1.5406$ Å) in the 2θ range of 5–90° with a scan rate of 6℃/min. The morphological investigation of the prepared sample was carried out with scanning electron microscopy (SEM) using JEOL JSM-IT200. The FTIR spectra were used to know about the functional groups characteristics of the samples using FTIR spectrometer 4600, Jasco, Japan. The formation of the porous carbon framework was determined using Raman spectroscopy (Renishaw INVIA 0120–20, UK). X-ray photoelectron spectroscopy (XPS) used to record surface chemical composition by using, ULVAC-PHI500 Version Probe III, Inc. The specific surface area and total pore volume of the sample analysis, it was studied on the Brunauer-Emmet-Teller (BET, BELSORP-mini II, Bel Japan Inc., Japan). Thermogravimetric analysis (TGA) of the prepared sample was carried out on Hitachi STA 7300 instrument with a heating rate of 10℃/min under an N_2 gas environment.

2.4 Electrochemical measurement

The electrochemical performance of the synthesized materials was recorded on CHI660E electrochemical workstation by three electrode systems in 1.0 M KOH solution. All the measurements were carried out using a graphite rod as a counter and aqueous Ag/AgCl (3 M KCl) as a reference electrode. To get catalyst ink, 4 mg of the prepared catalyst was dispersed in a 1 mL solution containing 200 μL IPA, 796 μL DI water, and 4 μL Nafion (5 wt% Sigma Aldrich) followed by ultra-sonication for 1 h in the ice-cold bath. Then, 4 μL of this catalyst ink was coated on a Ni-foam substrate (0.2×0.2 cm^2) and after drying served as a working electrode. Initially, the coated Ni-foam electrode surface was electrochemically pre-activated using cyclic voltammetry (CV), by cycling between -0.4 to 0.3 V vs. Ag/AgCl in N_2 saturated 1.0 M KOH solution at a scan rate of 100 mV/s. Linear sweep voltammetry (LSV) performance was recorded at a scan rate of 10 mV/s. All potential values were converted into reversible hydrogen electrode (RHE) by equation $E_{RHE} = E_{Ag/AgCl} + 0.197 + 0.059 \times pH$. The electrochemical impedance spectroscopy (EIS) performance was recorded in the frequency range of 100 kHz to 0.01 Hz at $\eta = 310$ mV. The Tafel slope was obtained from the LSV curves by plotting overpotential (η) vs log (J). The catalytic stability of the electrocatalyst was also recorded by the chronoamperometric (i-t) technique.

3 Results and discussion

3.1 Structural and morphological properties

Initially, CuBTC was synthesized by a hydrothermal method and then transformed to porous Cu emmbeded carbon, CuBTC C400, CuBTC C600, and CuBTC C800 by pyrolysis in an N_2 atmosphere at 400, 600, and 800℃, respectively. To explore the thermal stability of the CuBTC, TGA was carried out in the range of 25–1000℃ under an N_2 atmosphere (Fig. 1). The two main weight losses are observed in the CuBTC, in the first stage nearly, 35% weight loss was observed at 120℃, owing to the removal of weakly adsorbed water molecules [19]. Whereas in the second stage nearly 60% weight loss was observed from 240 to 380℃, it might be due to loss of BTC molecule with the release of O_2. The O_2 reacts with Cu resulting into hybrid Cu_2O/Cu mixed phase [20], due to the simultaneous liberation of reducing gases, such as CO, CH_4, and H_2 during pyrolysis [21]. From investigation of TGA sudden weight loss up to 380℃ validates the selection of pyrolysis temperature to be 400, 600, and 800℃. The hybrid phase of Cu_2O/Cu well confirmed in XRD analysis [22].

The XRD pattern of the pyrrolyzed samples and pristine CuBTC are shown in Fig. 2a. However the corresponding (222) crystal plane of CuBTC obtained at 11.77°, which is significantly sharp exhibited the good crystallinity of the CuBTC [23]. However, the pyrolyzed sample CuBTC C400 shows less intense peak of Cu_2O for (111) crystal plane obtained at 36.6°. The CuBTC C800 exhibits characteristic peaks of Cu_2O for (111), (200), and (220) located
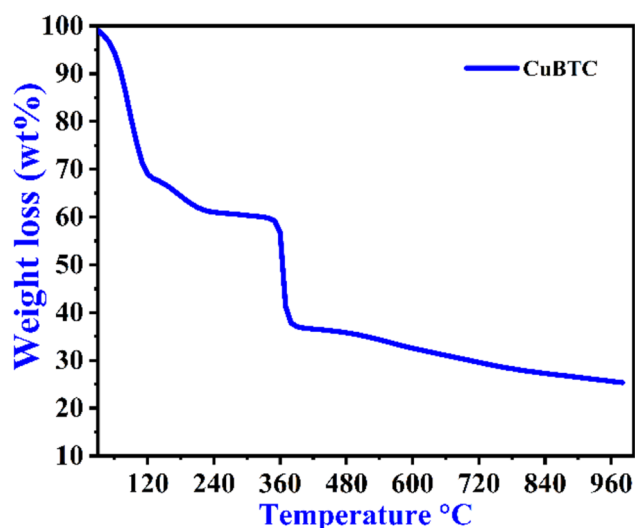
Fig. 1 Thermogravimetric (TGA) curve for as synthesized CuBTC

at 36.5, 43.0, and 61.0°, respectively. From XRD analysis, it is observed that there is formation of hybrid Cu_2O/Cu pattern in CuBTC C600 as evidenced by the appearance of sharp peaks at 2θ values of 36.5, 43.2, 61.3, and 74.1° associated with crystal planes (111), (200), (220), and (311) for Cu_2O respectively [21]. Although, the characteristic peak of Cu NPs of (200) crystal plane obtained at 50.4° in CuBTC C600 [24].

The FTIR spectrum was used to know the functional groups present into the prepared materials shown in Fig. 2b [25]. The CuBTC exhibits that the peaks at 729 cm^{-1} can be ascribed to the stretching vibration of the C–Cu–O bond and 1371 and 1450 cm^{-1} illustrates to the asymmetric stretching vibrations of carboxylate ions. The peak at 1647 cm^{-1} belongs to symmetric stretching vibration of carboxylate ion, which differ from the peak at 1720 cm^{-1} in H_3BTC, due to the oxygen atoms in the carboxyl groups attached with Cu^{+2}. The broad band appears at the 2700–3600 cm^{-1} indicates the $-OH$ group present in the carboxylic acid [26]. After pyrolysis at various temperature the peaks are shifted to 623 cm^{-1}, the intense peak at 623 cm^{-1} confirmed Cu–O stretching vibration [27]. Additionally, to evaluate the state of the carbon in the materials, Raman spectra (Fig. 2 e) were recorded. The two distinctive peaks are observed at 1385 and 1595 cm^{-1}, which correspond to the D and G bands respectively. The intensity of the G band is higher than the D band. The D band is caused by defects in Raman characteristics and the G band is related to the sp^2 carbon atoms in-plane vibrations which confirms the formation of porous carbon [28]; however, the intense peaks in CuBTC C600 shows as compared to CuBTC C400 and 800 implies porous nature which helps to optimise the pyrolysis temperature.

The SSA and porosity of CuBTC and the pyrolyzed samples were characterized using the N_2 adsorption/desorption profiles in Fig. 2 c, b, d. The CuBTC showed type I isotherm with presence of mesopores and all pyrolyzed samples showed type I isotherm with H4 hysteresis loop indicated the occurrence of meso-micropores. The textural properties of the prepared samples are showed in Table 1. It could be seen that CuBTC possessed the highest SSA (1773.4 m^2g^{-1}) with 0.7119 cm^3g^{-1} pore volume and 1.6057 nm pore diameter which was reliable with the mesoporous assembly [29]. The SSA after pyrolysis at altered temperatures were highly diverse from CuBTC. The low pyrolysis temperature is not enough for formation of porous carbon; however, high pyrolysis temperature was attributed to the collapse of part of the pore structure, which has great agreement with SEM images. The CuBTC C600 had an SSA of 46.16 m^2g^{-1} and a pore volume of about 0.053091 cm^3g^{-1}. The results confirmed that CuBTC C600 had abundant meso-micro pore structure, which favours enhanced active sites, and improved the electrochemical activity. For as synthesized materials, namely CuBTC and Cu-embedded porous carbon, which were produced at different pyrolytic temperatures, the percentage of porosity, which includes micro-, meso-, and macro-porous structures, was measured. The larger SSA was mainly attributed to the predominance of microporosity in comparison to meso- and macroporosity [30]. Remarkably, the material obtained from the pyrolysis of CuBTC at 400 °C showed a virtually equal distribution of micro- and mesoporous structures, as demonstrated by the decrease in SSA (58.48 m^2g^{-1}). As compared to CuBTC C800, the sample CuBTC C600 provides better lattice sites. for the dispersion of Cu_2O and Cu nanoparticles at particular percentages of microporosity (32.8%), mesoporosity (58.7%), and macroporosity (8.4%) (Table 1) [31] which desired to improve the electrocatalytic activity.

The SEM micrographs of the CuBTC shows a constant and structured octahedral structure as shown in Fig. 3. After high pyrrolyzed temperature, the octahedron structure is well preserved in CuBTC C600, showing the compressed phase of structural integrity of the porous octahedron carbon frame as shown in Fig. 4 [21]. During pyrolysis, Cu and Cu_2O NPs are embedded in the porous carbon framework forming in the CuBTC C600. The SEM images clearly shows the morphology progression of the CuBTC to CuBTC C800 (ESI Fig. S1-S2). Notably, the smooth surface of the CuBTC converts in to porous CuBTC C600, and at high temperature release of gases causes thermal decomposition in CuBTC owing to the ligands and the unequal substitution of Cu destroys surface morphology in CuBTC C800.

XPS analysis was performed to probe the depth of surface chemical composition of synthesized CuBTC C600, which are quite sensitive to oxidation states. The performance of the XPS analysis demonstrates that in Fig. 5a, b, c, d, where,
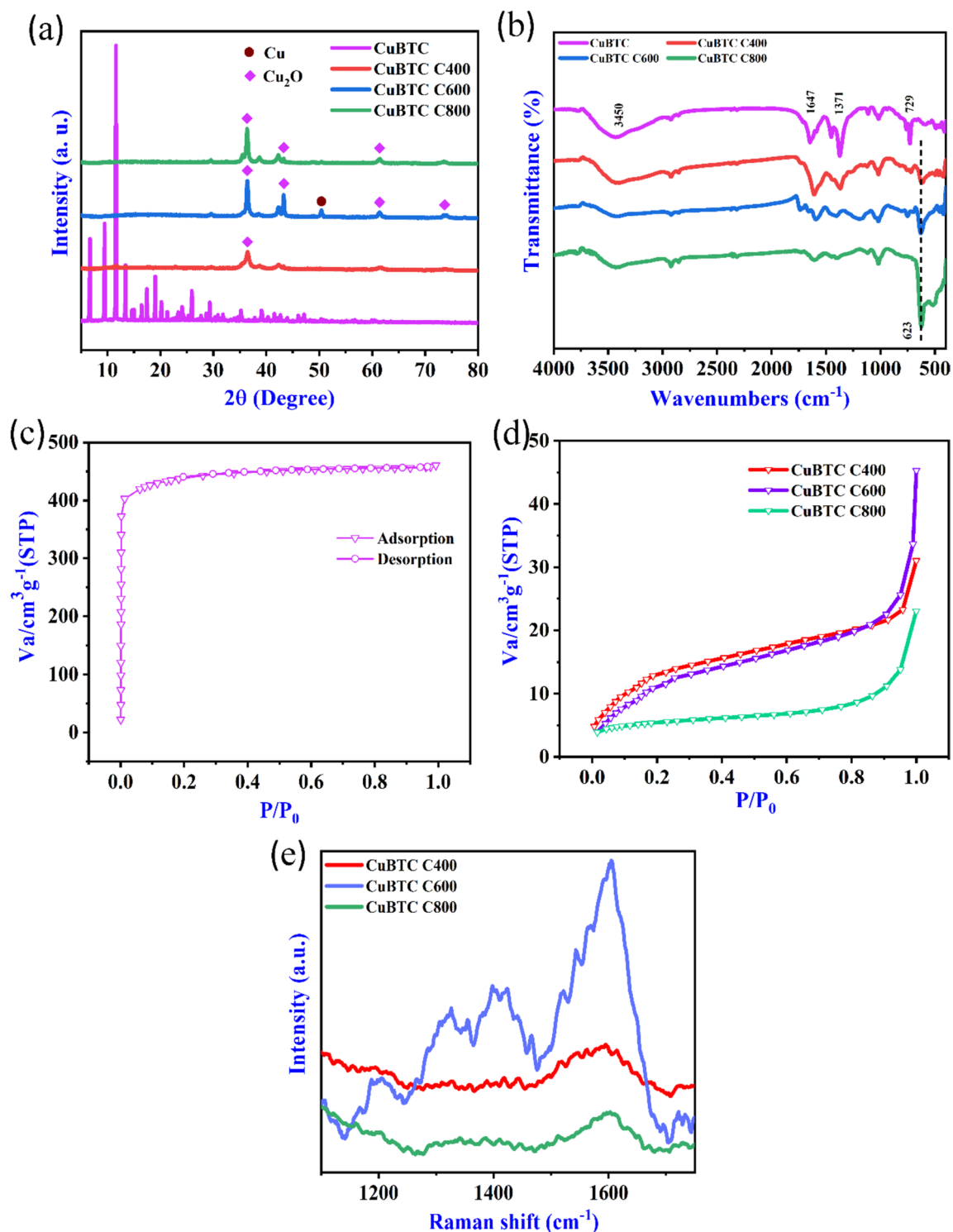
Fig. 2 **a** Comparative XRD of CuBTC and the samples prepared by pyrolyzing CuBTC at different temperatures; **b** the FT-IR spectra; **c** N$_2$ adsorption–desorption isotherm plots of CuBTC; **d** porous carbon samples; and **e** Raman spectra of CuBTC-derived carbons

surveys spectrum (Fig. 5a) clearly shows three pronounced peaks corresponding to the elements Cu, C, and O. The O1s spectrum can be deconvoluted into three peaks at 529.74, 531.33 and 533.52 eV in Fig. 5b, which are assigned to

the Cu–O, C=O, and C-O respectively. In the spectra of C1s (Fig. 5c), the peaks display binding energy at around 284.61, 286.13, and 288.20 eV demonstrate that the presence of C–C, C-O, and O-C=O respectively, specify the

Table 1 The consonant textural properties specific surface area (SSA); total pore volume (V_t); pore volume (V_p) of the Cu BTC, Cu BTC C400, Cu BTC C600, and Cu BTC C800 samples

Sample name	SSA (m^2g^{-1})	V_t (cm^3g^{-1})	V_p (cm^3g^{-1})	Porosity (%)		
				Micro	Meso	Macro
CuBTC	1773.4	0.7119	0.066367	96.98	2.64	0.37
CuBTC C400	58.48	0.045191	0.036059	48.00	44.45	6.77
CuBTC C600	46.16	0.053091	0.048562	32.87	58.67	8.45
CuBTC C800	19.36	0.03278	0.027303	9.02	79.91	11.06
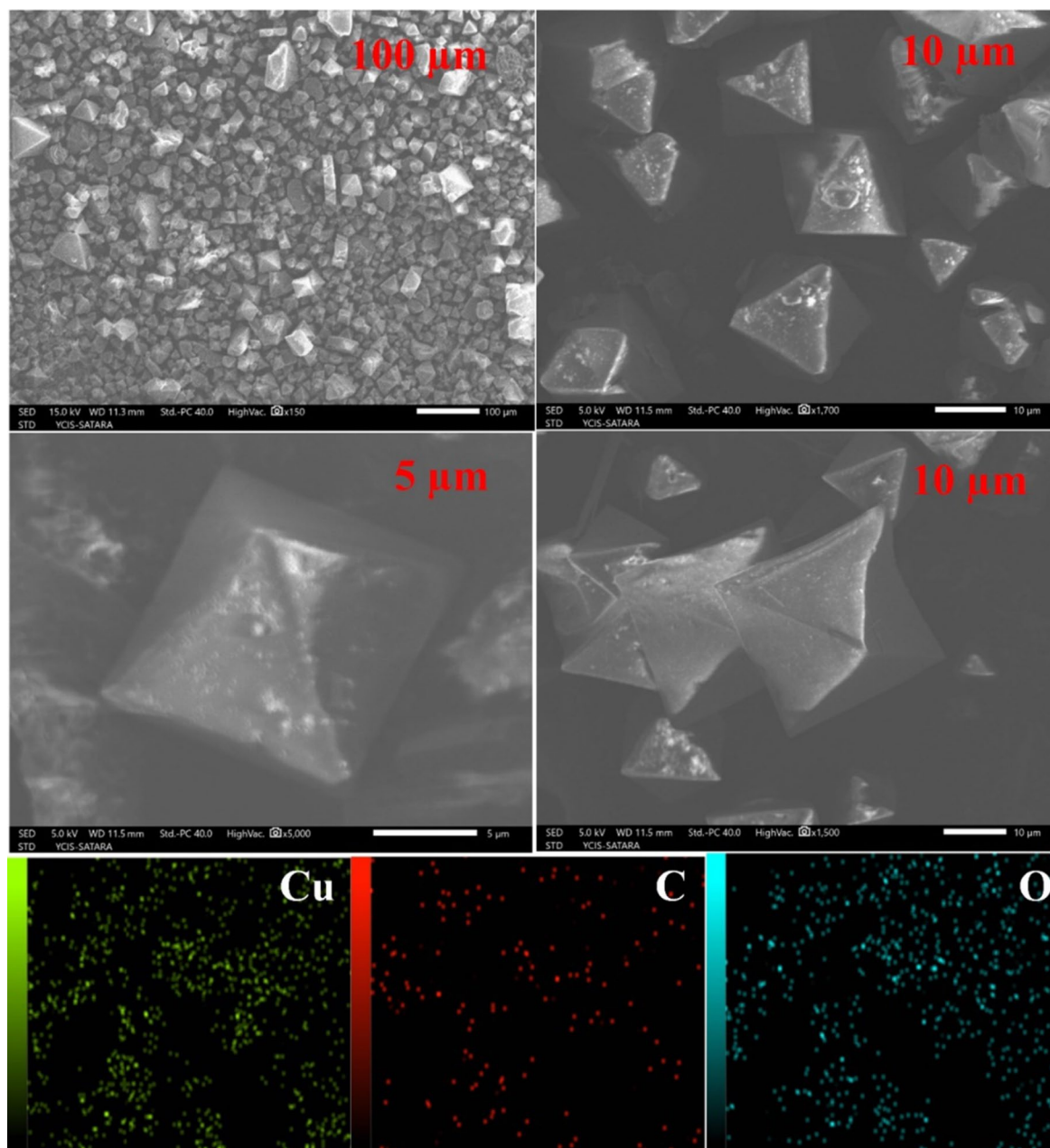
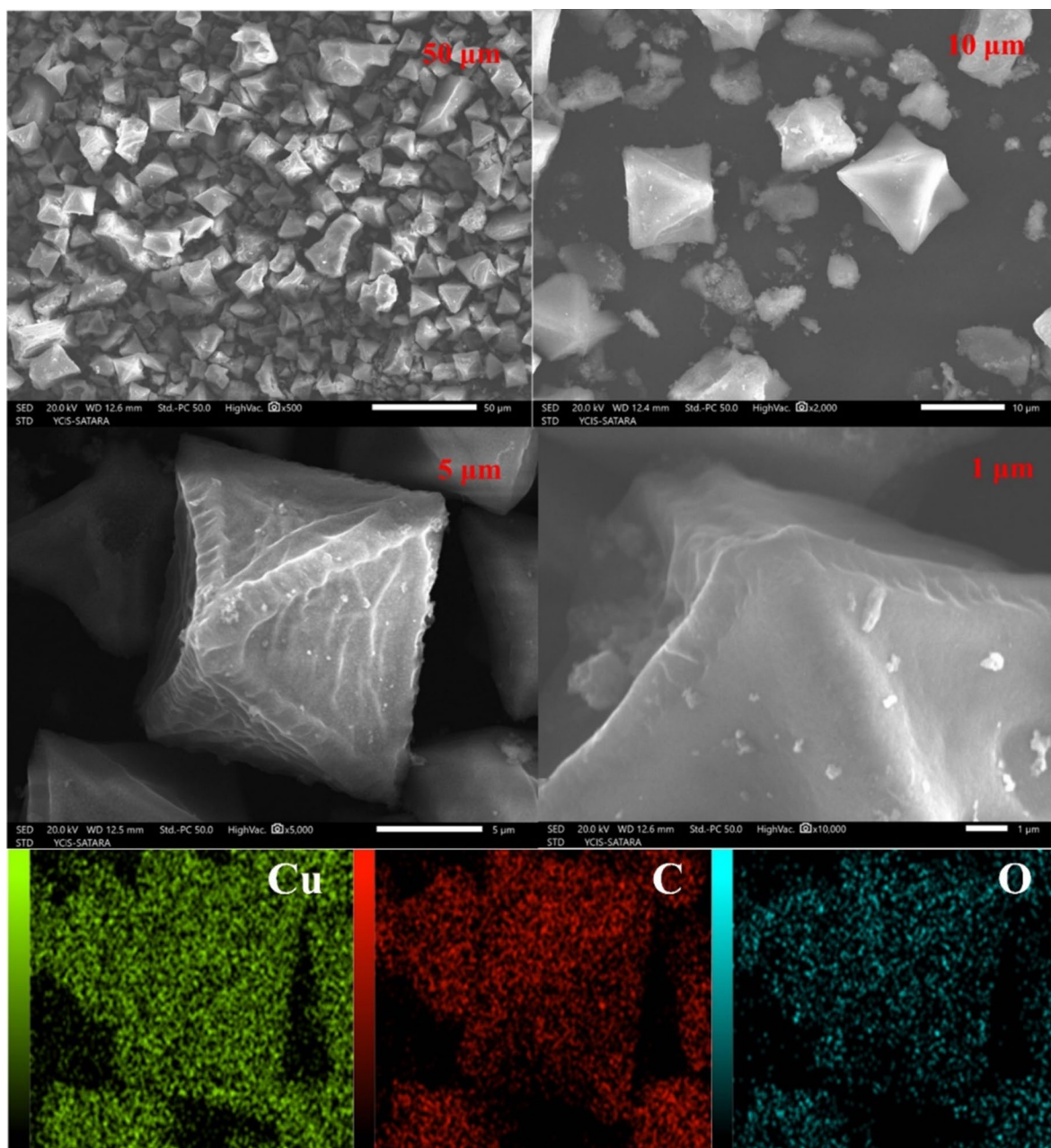**Fig. 3** SEM images of CuBTC and corresponding EDX elemental mapping

Fig. 4 SEM images of CuBTC C600 and corresponding EDX elemental mapping

presence of carbon [32, 33]. As observed in Fig. 5d, for Cu2p, the two unique peaks located at around 933.1 eV and 953.0 eV, respectively correspond to the Cu core spectra of $2p_{3/2}$ and $2p_{1/2}$. Furthermore, satellite peaks at 945.2 eV and 963.38 eV have been noted. These investigations suggest the existence of Cu with a oxidation state Cu^{1+} (Cu_2O) in CuBTC C600 [34, 35]. The full d shell of Cu_2O results forbiddance of screening via a charge transfer into the d state, which notably decreases the intensity of the satellite peak confirms the formation of Cu_2O [36] which is also supported by XRD analysis.

3.2 Electrocatalytic performance (OER)

The electrochemical performance of the CuBTC and its derived carbons towards OER has been investigated by CV and LSV at room temperature. Initially, prepared electrocatalysts loaded on Ni-foam electrodes (having a geometric area of 0.04 cm^2) were scanned nearly 100 cycles at 100 mV/s using CV in the range of -0.4 to 0.3 V vs. Ag/AgCl, for short-term stability. The oxygen evolution activity is studied by LSV and conducted using a standard three-electrode system at a scan rate of 10 mV/s in N_2 saturated 1.0 M KOH
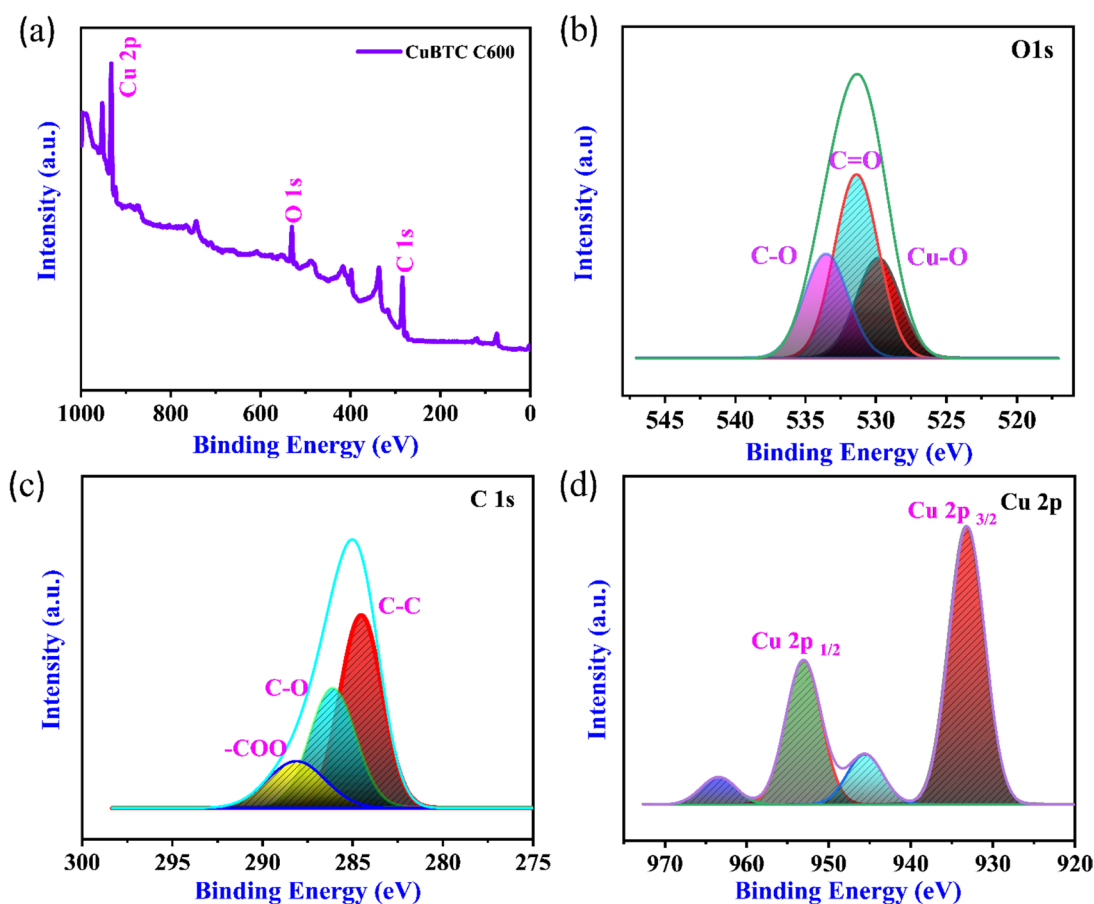
Fig. 5 XPS spectra of **a** survey scan, **b** O 1 s, **c** C 1 s, and **d** Cu 2p of CuBTC C600

electrolyte [37]. Accordingly, Fig. 6a illustrates the OER polarization curves of MOF-derived carbon at various temperatures, which shows a minimum overpotential of 310 mV (1.54 mV) at the current density of 10 mA/cm^2 for CuBTC C600, which is quite comparable with the other Cu-based catalysts shown in Table 2.

The results suggesting that the CuBTC C600 electrocatalyst has the highest OER activity among all other prepared materials attributed to the hybrid Cu$_2$O/Cu connected porous carbon form of the CuBTC C600 provides large channels for rapid electron transfer and beneficial for electrolyte penetration. Additionally, high intrinsic activity, active sites, superior mass/charge transport ratio, and easy release of oxygen bubbles contributes its electrocatalysis properties. It means that 600 °C pyrolysis temperature attain the desired activity for OER.

Additionally, to examine the kinetics performance of the CuBTC C600 by the corresponding Tafel plots (η versus log j), shown are calculated by using the LSV curves as stated to the Tafel equation $\eta = b \log j + a$, where j is the current density and b is the Tafel slope. The Tafel slope of CuBTC C600 (80 mV dec^{-1}) is exhibited in Fig. 6b and is

much lower than those of other electrocatalysts, indicating favourable reaction kinetics compared to other electrocatalysts [47]. The electrocatalyst at the electrode and electrolyte interface, EIS was applied, which gives valuable information about the electrocatalyst [2]. As shown in Fig. 6c, the EIS investigation for all CuBTC-derived carbon catalysts was recorded from 100 kHz to 0.01 Hz, with an amplitude of 0.005 V in a 1.0 M KOH solution. The lower and higher frequencies of the Nyquist plots demonstrate the charge transfer resistance (R_{ct}) and solution resistance (R_s) respectively. As a result, the CuBTC C600 shows the smallest charge transfer resistance compared to all other catalysts, indicating its electronically more conductive behavior, which is favorable for OER. The electrocatalytic activity, stability and durability of the electrocatalyst are vital aspects required for OER. The chronoamperometric (i-t) curve measurements in Fig. 6d were further studied for long-term electrochemical stability performance for CuBTC C600 in 1.0 M KOH solution [48]. After 12 h of continuous operation, no changes were observed in current density at the overpotential of 310 mV. The result shows the good stability of the CuBTC C600 electrocatalyst. However, the initial drop in
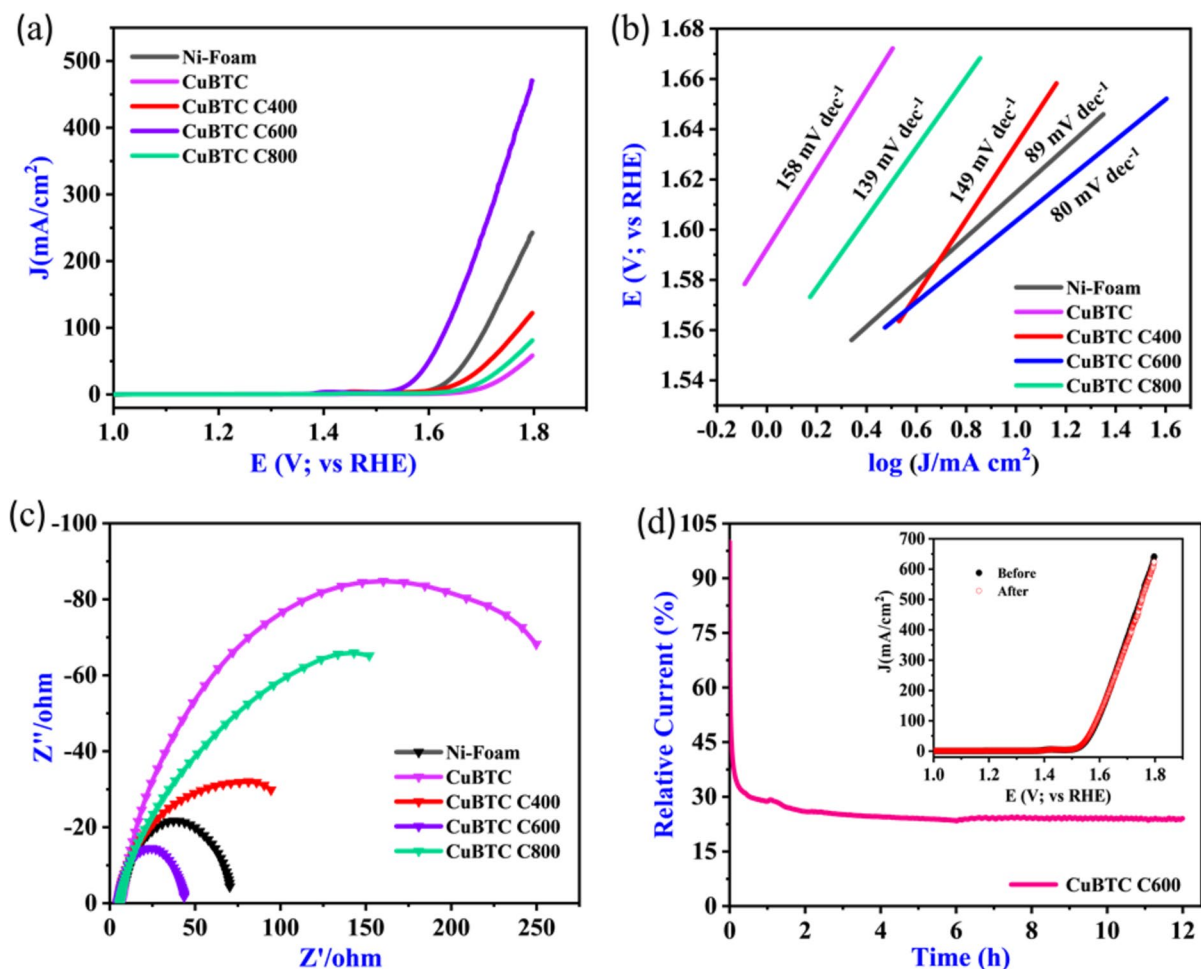
Fig. 6 Comparative OER performance of CuBTC materials: **a** LSV curves; **b** corresponding Tafel slopes; **c** EIS spectra, and **d** chrono-amperometric stability test of CuBTC C600 catalyst for 12 h, whereas inset shows the polarization curves of CuBTC C600 before and after chronoamperometric stability test

Table 2 Comparison of OER activity for various Cu-based samples reported in literature

Catalyst	Overpotential (η) at 10 mA/cm^2	Tafel slope (mVdec^{-1})	Substrate	Electrolyte	Ref
CuCo-MOF	340	173.5	Carbon fiber	1.0 M KOH	[38]
CuCo-MOF	380	118	RDE	0.1 M KOH	[39]
$(Co_{0.21}Ni_{0.25}Cu_{0.54})_3Se_2$	272	53.3	Se film	1.0 M KOH	[40]
3D Cu (OH)$_2$-NWAs	530	86	CF film	0.1 M NaOH	[41]
NiFe/Cu$_2$O NWs/CF	215	42	CF film	1.0 M KOH	[42]
Ni-Cu NCs	150	120	GCE	1.0 M NaOH	[43]
MOF [Cu (OH)$_2$]	330	108	CF film	1.0 M KOH	[44]
M-NC-CoCu	310	77	Ni foam	1.0 M KOH	[45]
Cu/Cu$_2$O/CuO	289	-	CF film	1.0 M KOH	[46]
CuBTC C600	310	80	Ni foam	1.0 M KOH	This work

OER stability test (Fig. 6d) can be attributed to several factors related to the experimental conditions and the nature of oxygen evolution reactions. Here are some possible causes: (1) electrode activation: At the beginning, the electrode may still be undergoing the activation process, leading to a rapid drop in current. Once the activation process is complete, the current may stabilize; (2) surface passivation: the electrode/electrolyte interface can lead to the formation of

passivation layers (such as metal oxides or hydroxides) and this can impede the reaction kinetics, causing a decrease in current. As time passes, the passivation layer stabilizes, and the current may reach a stable; (3) the generation of oxygen gas bubbles at the electrode surface could be associated with the detachment of active material and hence affecting the electrochemical surface area (ECSA) and as a result decrease in the measured current. Of course, it is essential to carefully consider these factors and conduct further analyses to pinpoint the specific cause of the initial current drop. However, the exact mechanism of the initial current drop in the present study is still unclear and we would like to extend our experimental approach in this direction in future work.

4 Conclusion

In the present study, the synthesis of CuBTC MOF possessing high SSA (1773.4 m^{2}g^{-1}) is achieved. The obtained MOF war further pyrolyzed at different temperatures to obtain Cu-embedded porous carbon electrocatalysts under controlled N$_2$ atmosphere. From over all study, it is concluded that the SSA of the MOF decreases with increase in the pyrolysis temperature due to the formation of macropores. Further the sample CuBTC C600 showed a superior electrocatalysis performance as compared to the rest materials due to the hybrid Cu$_2$O/Cu connected porous carbon form provides large channels favourable for rapid electron transfer and beneficial for electrolyte penetration. Further, it showed the better electrocatalytic activity, long-term durability, and suitable reaction kinetics for OER in alkaline conditions. This study attributes that the pyrolysis temperature 600℃ is favorable to convert the MOFs into metal-embedded porous carbonaceous catalyst. This work will provide the pathway for researchers to develop metal oxide/metal-embedded porous carbonaceous electrocatalyst for OER as well as other catalytic applications.

Declarations

Competing interests The authors declare no competing interests.

References

1. P. Wang, S. Zhang, Z. Wang, Y. Mo, X. Luo, F. Yang, M. Lv, Z. Li, X. Liu, J. Mater. Chem. A. **11**, 5476 (2023)
2. A.H. Al-Naggar, N.M. Shinde, J.-S. Kim, R.S. Mane, Coordination Chemistry Reviews **474**, 214864 (2023)
3. I. PATIL, P. Marbaniang, A. Swami, C.M. Enoch, S. Ingavale, J. Mater. Chem. A. **11**, 21780 (2023)
4. R. Samal, P.V. Shinde, C.S. Rout, Emergent Materials **4**, 1047 (2021)
5. A. Koli, A. Kumar, A. Pattanshetti, A. Supale, K. Garadkar, J. Shen, J. Shaikh, S. Praserthdam, R.K. Motkuri, S. Sabale, ChemPlusChem. **e202300373**, 1 (2023)
6. C. Yuan, H. B. Wu, Y. Xie, and X. W. (David) Lou, Angew. Chem. Int. Ed. **53**, 1488 (2014).
7. Q. Wang, D. Astruc, Chemistry Reviews **120**, 1438 (2020)
8. S. Sabale, D. Barpaga, J. Yao, L. Kovarik, Z. Zhu, S. Chatterjee, B.P. McGrail, R.K. Motkuri, X.-Y. Yu, A.C.S. Appl, Materials Interfaces **12**, 5090 (2020)
9. K. Sharma, V. Hasija, S. Patial, P. Singh, V.-H. Nguyen, A.K. Nadda, S. Thakur, P. Nguyen-Tri, C.C. Nguyen, S.Y. Kim, International Journal Hydrogen Energy **48**, 6560 (2023)
10. H.-F. Wang, L. Chen, H. Pang, S. Kaskel, Q. Xu, Chemical Society Reviews **49**, 1414 (2020)
11. C. Xu, L. Liu, C. Wu, K. Wu, Sensors and Actuators B Chemical **310**, 127885 (2020)
12. J. Gao, P. He, T. Yang, X. Wang, L. Zhou, Q. He, L. Jia, H. Deng, H. Zhang, B. Jia, X. He, Journal Electroanal Chemistry **861**, 113954 (2020)
13. M. Wang, M. Lin, J. Li, L. Huang, Z. Zhuang, C. Lin, L. Zhou, L. Mai, Chemical. Communication **53**, 8372 (2017)
14. S.R. Sabale, J. Zheng, V.R.S. Vemuri, X.-Y. Yu, B.P. McGrail, R.K. Motkuri, Synth. Catal. **1**(1), 5 (2016)
15. C. Zhang, J. Xiao, X. Lv, L. Qian, S. Yuan, S. Wang, P. Lei, Journal Materials Chemistry A **4**, 16516 (2016)
16. A. Koli, A. Pattanshetti, S. Mane-Gavade, R. Dhabbe, R. Kamble, K. Garadkar, S. Sabale, Waste Manag. Bull. **1**, 97 (2023)
17. M. Iwanow, T. Gärtner, V. Sieber, B. König, Beilstein Journal Organic Chemistry. **16**, 1188 (2020)
18. K. Schlichte, T. Kratzke, S. Kaskel, Microporous Mesoporous Mater **73**, 81 (2004)
19. G.A. Bodkhe, B.S. Hedau, M.A. Deshmukh, H.K. Patil, S.M. Shirsat, D.M. Phase, K.K. Pandey, M.D. Shirsat, Front. Chemistry. **8**, 803 (2020)
20. R. Nivetha, A. Sajeev, A.M. Paul, K. Gothandapani, S. Gnanasekar, P. Bhardwaj, G. Jacob, R. Sellappan, V. Raghavan, K.C. N, S. Pitchaimuthu, S.K. Jeong, A.N. Grace, Mater. Res. Express. **7**, 114001 (2020)
21. A. Jalal, Y. Zhao, A. Uzun, Industrial Engineering Chemistry Research **61**, 2068 (2022)
22. H. Xu, J.-X. Feng, Y.-X. Tong, G.-R. Li, ACS Catalysis **7**, 986 (2017)
23. J. Zhao, W.T. Nunn, P.C. Lemaire, Y. Lin, M.D. Dickey, C.J. Oldham, H.J. Walls, G.W. Peterson, M.D. Losego, G.N. Parsons, Journal of the American Chemical Society **137**, 13756 (2015)
24. J. Shanmugapriya, C.A. Reshma, V. Srinidhi, K. Harithpriya, K.M. Ramkumar, D. Umpathy, K. Gunasekaran, R. Subashini, Journal Nanomaterials **2022**, 7967294 (2022)
25. S.A.M. Rizvi, N. Iqbal, M.D. Haider, T. Noor, R. Anwar, S. Hanif, Catalysis Letters **150**, 1397 (2020)
26. P. Gao, X.-Y. Sun, B. Liu, H.-T. Lian, X.-Q. Liu, J.-S. Shen, Journal Materials Chemistry C **6**, 8105 (2018)
27. C. Chen, H. Xu, L. Xu, F. Zhang, J. Dong, H. Wang, RSC Advances **3**, 25010 (2013)

28. D. Momodu, M. Madito, F. Barzegar, A. Bello, A. Khaleed, O. Olaniyan, J. Dangbegnon, N. Manyala, Journal Solid State Electrochemistry **21**, 859 (2017)

29. Y. Liu, S. Liu, A.A.S. Gonçalves, M. Jaroniec, RSC Advances **8**, 35551 (2018)

30. S.M. Varghese, A.R. Chowdhury, D.N. Arnepalli, G.R. Rao, Carbon Trends **10**, 100250 (2023)

31. J. Wang, Y. Chen, S. Zhang, C. Yang, J.-Y. Zhang, Y. Su, G. Zheng, X. Fang, Small **18**, 2202238 (2022)

32. H. Li, J. Qin, Y. Zhang, S. Xu, J. Du, J. Tang, RSC Advances **8**, 39352 (2018)

33. S. Shams, W. Ahmad, A.H. Memon, Y. Wei, Q. Yuan, H. Liang, RSC Advances **9**, 40845 (2019)

34. X. Xiong, C. You, Z. Liu, A.M. Asiri, X. Sun, A.C.S. Sustain, Chemical Engineering **6**, 2883 (2018)

35. A.M. Abdel-Mageed, B. Rungtaweevoranit, M. Parlinska-Wojtan, X. Pei, O.M. Yaghi, R.J. Behm, Journal of the American Chemical Society **141**, 5201 (2019)

36. T. Ghodselahi, M.A. Vesaghi, A. Shafiekhani, A. Baghizadeh, M. Lameii, Applied Surface Science **255**, 2730 (2008)

37. Z. Xu, C.-L. Yeh, Y. Jiang, X. Yun, C.-T. Li, K.-C. Ho, J.T. Lin, R.Y.-Y. Lin, A.C.S. Appl, Materials Interfaces **13**, 28242 (2021)

38. Q. Liu, J. Chen, F. Yu, J. Wu, Z. Liu, B. Peng, New Journal Chemistry **45**, 16714 (2021)

39. J. Zhang, C. Zhang, X. Duo, Z. Liu, C. Liu, L. Guo, A. Xie, S. Luo, Ionics **26**, 5123 (2020)

40. X. Cao, E. Johnson, M. Nath, Journal Materials Chemistry A **7**, 9877 (2019)

41. C.-C. Hou, W.-F. Fu, Y. Chen, Chemsuschem **9**, 2069 (2016)

42. H. Chen, Y. Gao, L. Sun, Chemsuschem **10**, 1475 (2017)

43. R.P. Gautam, H. Pan, F. Chalyavi, M.J. Tucker, C.J. Barile, Catalysis Science and Technology **10**, 4960 (2020)

44. H. Li, Y. Liu, F. He, H. Yang, Z. Li, Q. Zhou, K. Tang, International Journal Hydrogen Energy **45**, 21540 (2020)

45. A. Macedo Andrade, Z. Liu, S. Grewal, A.J. Nelson, Z. Nasef, G. Diaz, M.H. Lee, Dalton Trans. **50**, 5473 (2021)

46. R. Li, J. Xu, R. Zeng, Q. Pan, T. Tang, W. Luo, Journal Power Sources **457**, 228058 (2020)

47. S. Pavithra, V.K. Jothi, A. Rajaram, S. Ingavale, A. Natarajan, Energy Fuels **36**, 6409 (2022)

48. Y. Li, H. Xu, H. Huang, L. Gao, Y. Zhao, T. Ma, Electrochemistry Communications **86**, 140 (2018)